UNIVERSITÀ DEGLI STUDI DI PADOVA

Dipartimento di Fisica e Astronomia "Galileo Galilei"

Master Degree in Physics

Master's Degree dissertation

Intra-cavity optical and mechanical dissipation of a coating membrane for gravitational wave detectors

Supervisor:

Prof. Marco Bazzan

Co-supervisor:

Prof. Jean-Pierre Zendri

Student:

Nicole Busdon

Academic Year 2022/2023

Acknowledgements

Contents

Introduction

Gravitational wave interferometers are highly sensitive scientific instruments. Recent progress in gravitational wave research has led to significant discoveries and expanded our understanding of the Universe. One of the most crucial parts of the interferometers are their mirror test masses. The research work of this thesis is therefore driven by the aim to study the thermal noise of the highly reflective mirror coatings that is expected to limit the sensitivity of the next generation of gravitational wave detectors. Indeed, gravitational wave interferometers have to ensure a very low displacement noise, a condition that is mainly undermined by the Brownian noise of the coating. The latter can be related to the mechanical dissipations of the coating material through the fluctuation-dissipation theorem when the system is at thermal equilibrium. This fundamental noise limits the interferometer sensitivity in its most sensitive detection band between 20 and 1000 Hz, therefore it is extremely important to significantly reduce the coating thermal noise to enable the detection of a wider range of cosmological sources emitting in this range.

Furthermore the coatings have to possess extreme transparency at the operation wavelength, in order not to interact in unwanted ways with the high-power laser circulating into the interferometer. The coating used in present gravitational wave instruments are multilayers of amorphous oxides such as Tantala (Ta_2O_5) and Silica (SiO_2). One of the main challenges nowadays is the development of new materials with an extremely low level of mechanical and optical losses. Furthermore, with the advent of the next-generation interferometers such as Einstein Telescope, new coatings need to be developed in order to operate at different wavelengths as well as in non-standard (cryogenic) conditions.

However, both of these dissipations (mechanical and optical) are so small that they are difficult to be measured on optical coatings using standard approaches. Moreover, it is highly desirable to have the possibility to perform such a delicate characterization in a wide temperature range going from room temperature to few Kelvins, in order to evaluate the energetics of the processes responsible for the thermally activated fluctuations.

At the present, optical losses are mainly characterized by means of pump-probe setups exploiting the photothermal effect induced by tiny absorption levels. On the other hand, mechanical losses are evaluated by measuring the ring-down time of a substrate coated with the material to be measured and set in vibration. This technique exploits a Gentle Nodal Suspension (GeNS) system to hold the sample without damping its oscillation. The mechanical losses of the coating are evaluated by comparing the losses of the sample with those of the pristine substrate, prior to the coating deposition. This technique is effective at room temperature, but when it comes to measurement at cryogenic temperatures it is very difficult to perform the analysis because the thermo-elastic interaction between the coating and the substrate heavily affects the results of the measurement at low temperatures. This problem so far has not been solved yet, so that a precise characterization technique for coating mechanical losses in a wide temperature range is not available yet.

This thesis project has the aim to develop an innovative experimental setup to measure both the optical losses and the mechanical dissipations of a freestanding coating membrane, both at room temperature and in cryogenic conditions. In our apparatus, the coating to be measured is not deposited on a substrate, but is rather suspended in the form of a thin membrane. The advantage

of this approach is that the thermo-elastic interaction between the coating and the substrate is nearly absent, allowing to extract meaningful data in the whole range between room temperature and few Kelvins.

The experimental apparatus includes a low-vibration cryostat, inside of which an optical cavity will be installed. The measurement consists in placing the membrane inside the resonator so that it couples with the stationary electromagnetic field circulating inside the cavity. The strength of the interaction depends on the membrane position with respect to the maxima and minima pattern of the electromagnetic field. For this reason the optical losses can be measured by monitoring the finesse of the Fabry- Perot cavity as a function of the membrane position along the optical axis. The mechanical dissipation will be measured instead using the dependence of the on resonance output power from the displacement of the membrane and transducing the vibrational signal of the membrane into an optical signal.

The first membranes to be tested are low-stress silicon nitride (SiN) membranes fabricated by a private company (Norcada). The choice of SiN is due to the fact that it is known to achieve very low mechanical dissipations but its optical losses are not yet characterized in depth as a function of stoichiometry and fabrication process. Furthermore, silicon nitride is one of the candidate materials to replace Ta2O5 in the Bragg mirrors of the gravitational wave interferometers.

In this thesis it will be reported the design and the realization of a first prototype set-up based on the above-mentioned scheme. While the measurement of the optical losses has not yet yielded definitive results, the preliminary behavior exhibited by the data collected up to this point appears to offer promising signs that the experimental setup is functioning effectively. The next steps will be focused on optimizing the apparatus and developing the instrumentation to measure the mechanical dissipation too.

Chapter 1

Gravitational waves: theory and detection

The existence of Gravitational Waves (GW) is a consequence of General Relativity and was predicted by Albert Einstein in 1916. This theory relates the curvature of the space-time with the energy-matter distribution, indeed GWs are perturbations of the metric (geometry of the space-time) that are caused by a movement of mass and which propagate at the speed of light. In this chapter their basic properties and their detection system will be described. The first detection of a GW was made on September 14th of 2015 by the LIGO-Virgo collaboration with the two Advanced LIGO detectors. It was emitted by the merger of a Binary Black Hole, providing the first direct proof of the existence of Black Holes. This event has marked the beginning of a new way of observing the Universe, and many detections have been done since then.

1.1 Gravitational waves theory

1.1.1 Einstein field equations

In the Theory of General Relativity, the Einstein field equations relate the local curvature of spacetime, described by the metric tensor, with the local distribution of energy and momentum, expressed by the stress-energy tensor $T_{\mu\nu}$ [1]:

$$R_{\mu\nu} - \frac{1}{2}g_{\mu\nu}R = kT_{\mu\nu} \tag{1.1}$$

where $R_{\mu\nu}$ is the Ricci tensor, R is the Ricci scalar, $g_{\mu\nu}$ is the metric tensor and:

$$k = \frac{8\pi G}{c^4} \tag{1.2}$$

Due to symmetry arguments Equation 1.1 reduces to a system of ten coupled differential equations and, thanks to their tensorial form, the equations are invariant for changes of coordinates. Gravitational waves are ripples in the space time curvature and their propagation in empty space ($T_{\mu\nu} = 0$) can be described by the Einstein field equations in the weak field approximation, namely when:

$$g_{\mu\nu} \simeq \eta_{\mu\nu} + h_{\mu\nu}, \qquad |h_{\mu\nu}| \ll 1 \tag{1.3}$$

where:

$$\eta_{\mu\nu} = \begin{pmatrix} -1 & 0 & 0 & 0 \\ 0 & 1 & 0 & 0 \\ 0 & 0 & 1 & 0 \\ 0 & 0 & 0 & 1 \end{pmatrix} \tag{1.4}$$

is the Minkowsky metric tensor.

This approximation holds in regions where the gravitational effects are relatively weak, thus the spacetime curvature is small and the solution can be derived using a perturbative approach.

The choice of this reference frame breaks the invariance of GR under coordinate transformation, leaving only one residual degree of freedom. By expanding the Ricci tensor at first order in h, it is possible to retrieve the following linearized wave equation [1]:

$$\Box h_{\mu\nu} + \partial_\mu \partial_\nu h - \partial_\mu \partial^\sigma h_{\sigma\nu} - \partial_\nu \partial^\sigma h_{\sigma\mu} = 0 \tag{1.5}$$

The remaining degree of freedom can be used to apply the additional coordinate transformation:

$$\tilde{x}^\mu \simeq x^\mu + \epsilon^\mu(x), \quad \text{with: } \epsilon^\mu \sim o(h) \tag{1.6}$$

in order to further simplify Equation 1.5.

Then, defining the trace reverse as:

$$\bar{h}_{\mu\nu} = h_{\mu\nu} - \frac{1}{2}\eta_{\mu\nu}h \tag{1.7}$$

and working in the De Donder gauge:

$$\Box \bar{h}_{\mu\nu} = 0 \tag{1.8}$$

the solution to the linearized wave equation can be written as a monochromatic plane wave using the Fourier decomposition:

$$\bar{h}_{\mu\nu}(x) = \Re\left(H_{\mu\nu}(k)e^{ik_\rho x^\rho}\right) \tag{1.9}$$

where $H_{\mu\nu} = H_{\nu\mu}$ is the polarization tensor and k^ρ is the wave vector.

This equation is valid only when the following conditions are fulfilled:

- The wave vector is null: $k^\rho k_\rho = 0$

- The De Donder condition is satisfied: $k^\rho H_{\mu\rho}(k) = 0$

Considering a frame in which the wave propagates along the z direction:

$$k^\mu = c\omega \begin{pmatrix} 1 \\ 0 \\ 0 \\ 1 \end{pmatrix} \tag{1.10}$$

it is easy to find that not all the elements of the polarization tensor are independent, and in particular $H_{3\mu} = H_{\mu3} = -H_{0\mu} = H_{\mu0}$. Therefore the polarization tensor results:

$$H_{\mu\nu} = \begin{pmatrix} H_{00} & H_{01} & H_{02} & -H_{00} \\ H_{01} & H_{11} & H_{12} & -H_{10} \\ H_{02} & H_{12} & H_{22} & -H_{20} \\ -H_{00} & -H_{10} & -H_{20} & -H_{00} \end{pmatrix} \tag{1.11}$$

7

At this point, with a quick calculation, it is possible to notice that H_{00}, H_{01}, H_{02} and $H_{11} + H_{22}$ are pure gauge degrees of freedom and they can be set to zero imposing the TT (traceless and transverse) gauge condition:

$$\begin{cases} H_{0\mu} = 0 \\ H_\mu^\mu = 0 \end{cases} \tag{1.12}$$

In this gauge $h_{\mu\nu} = \bar{h}_{\mu\nu}$, the polarization tensor reduces to two indipendent components, corresponding to two indipendent polarizations, and the final expression describing a gravitational wave propagating in the z direction is given by :

$$h_{TT}^{\mu\nu} = \begin{pmatrix} 0 & 0 & 0 & 0 \\ 0 & h_+ & h_\times & 0 \\ 0 & h_\times & -h_+ & 0 \\ 0 & 0 & 0 & 0 \end{pmatrix}_{\mu\nu} e^{i\omega\left(t-\frac{z}{c}\right)} \tag{1.13}$$

with wave vector $k = (\omega/c, 0, 0, k)$.

1.1.2 The effects of gravitational waves on test masses

The effect of gravitational waves on a mass distribution can be understood by analyzing the geodesic deviation of two infinitely close test masses [2], placed in the positions $x(\tau)$ and $x(\tau) + \xi(\tau)$ and subjected to the effect of a gravitational wave:

$$\frac{d^2\xi^\sigma}{d\tau^2} + 2\Gamma_{\mu\nu}^\sigma \frac{dx^\mu}{d\tau}\frac{d\xi^\nu}{d\tau} + \xi^\lambda \left(\partial_\lambda \Gamma_{\mu\nu}^\sigma\right) \frac{dx^\mu}{d\tau}\frac{dx^\nu}{d\tau} = 0 \tag{1.14}$$

Solving this equation in the TT gauge and at first order in h, one finds that apparently geodesics that are parallel at $\tau = 0$ remain parallel also afterwards:

$$\left.\frac{d\xi^j}{d\tau}\right|_{\tau=0} \quad \Rightarrow \quad \left.\frac{d^2\xi^j}{d\tau^2}\right|_{\tau=0} \tag{1.15}$$

where the index j indicates that we are considering only the spatial components.

This solution is due to the fact that in the TT gauge the coordinates are defined by freely falling particles and for this reason they are themselves deformed in presence of a gravitational wave. However, even though coordinate distances are not affected by gravitational waves, the effect on proper distances is instead visible.

For this calculation it is convenient to work using the Fermi local coordinates. In this reference frame the Christoffel symbols vanish at a chosen point (it is common to chose the origin), and the metric tensor at that point is the Minkowski metric. Using these hypothesis, along with the assumption that the particles move at non relativistic velocity:

$$\frac{dx^i}{d\tau} \ll \frac{dx^0}{d\tau} \tag{1.16}$$

Equation 1.14 can be simplified to the form:

$$\frac{d^2\xi^i}{d\tau^2} + \xi^j \left(\partial_j \Gamma_{00}^i\right) \left(\frac{dx^0}{d\tau}\right)^2 = 0 \tag{1.17}$$

As a tensor is invariant under changes of coordinates, using the form of the Riemann tensor in the TT gauge, the solution of Equation 1.17 is straightforward:

$$\ddot{\xi}^i = \frac{1}{2}\ddot{h}_{ij}^{TT}\xi^j \tag{1.18}$$

This means that the particles accelerate as if they were under the effect of a Newtonian force equal to:

$$F_i = \frac{m}{2}\ddot{h}_{ij}^{TT}\xi^j \tag{1.19}$$

Considering now a ring of particles displaced in the xy plane and a gravitational wave propagating in the z direction as described by Equation 1.13, it is easy to verify that there is no effect in the z direction:

$$\ddot{\xi}^i = \frac{1}{2}\ddot{h}_{3j}^{TT}\xi^j = 0 \tag{1.20}$$

Regarding instead the effect in the x and y directions it is necessary to analyze separately the effects of the plus and cross polarizations. Supposing that at a certain time t the separation between the two particles is $\xi(t) = (x_0 + \delta x(t), y_0 + \delta y(t))$ then:

- **Plus polarization:**

$$\begin{cases} \delta x(t) = \dfrac{1}{2}h_+ x_0 \cos(\omega t) \\ \delta y(t) = -\dfrac{1}{2}h_+ y_0 \cos(\omega t) \end{cases} \tag{1.21}$$

- **Cross polarization:**

$$\begin{cases} \delta x(t) = \dfrac{1}{2}h_\times y_0 \cos(\omega t) \\ \delta y(t) = \dfrac{1}{2}h_\times x_0 \cos(\omega t) \end{cases} \tag{1.22}$$
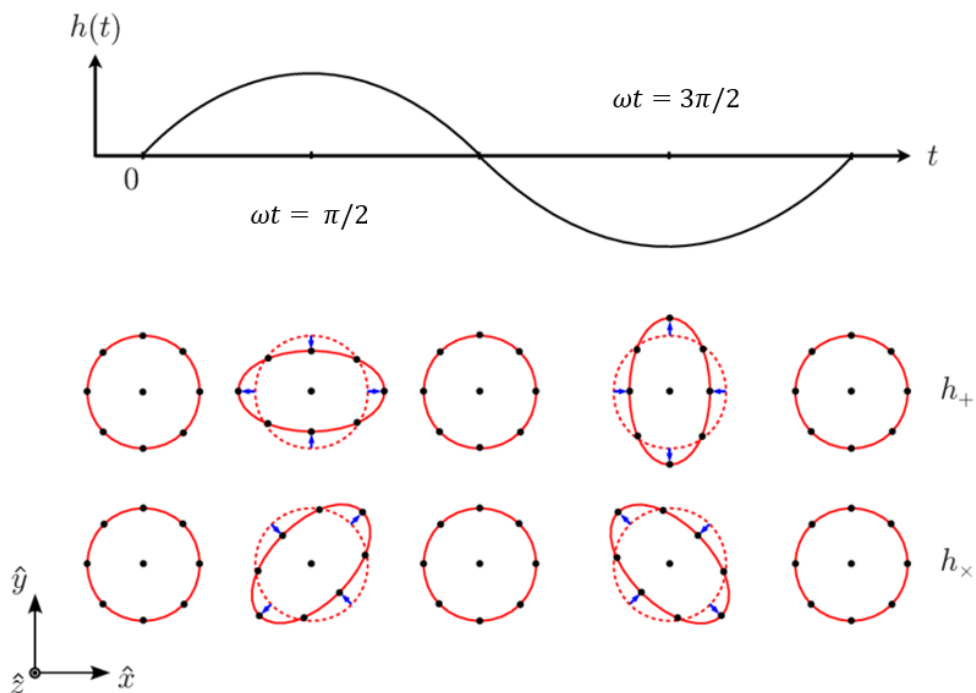

Figure 1.1: Effect of the plus and cross polarizations of a GW which propagates along the z axis through a ring of test masses.

From the last equations it is possible to understand that, for both polarizations, the distance between the test masses periodically contracts and then expands in one direction, while the opposite happens in the perpendicular direction. The effect of the two polarizations is identical if the axis are tilted by a $\pi/4$ angle and this is shown in Figure 1.1 along with the amplitude evolution of the GW with time.

1.2 Detection system

1.2.1 Gravitational waves interferometers

Different methods to detect gravitational waves have been implemented through the years: Weber Bars, Pulsar Timing Arrays, laser interferometry and, in the next future, space-based interferometers.

At present, the efforts of the scientific community are focused on the improvement of the ground-based gravitational waves interferometers. The working principle of these detectors is based on the fact that gravitational waves have two linear polarizations and that they produces tidal forces on any object or detector they interact with. If the object is small compared to the gravitational wave's wavelength, as in the case of ground-based interferometers, then relative to the object's center, the forces have the quadrupolar patterns shown in Figure 1.1.

The structure of the gravitational wave interferometer is designed to maximize this effect and for this reason, its structure consists of four test masses that, in pairs, form two long and perpendicular arms. The suspension system of the test masses is designed to guarantee the free falling condition by minimizing the action of any external force. To achieve this condition, each test mass is suspended to a pendulum chain equipped with a seismic isolation system and the whole structure is placed within high-vacuum; sophisticated feedback control systems are also implemented to monitor and adjust the position of the test masses. The layout of the detector is shown in Figure 1.2.

The interferometer test masses constitute the interferometer's input and end mirrors shown in Figure 1.2 and they form a Fabry-Perot cavity in each arm of the interferometer. The laser beam used to monitor the motion of the mirrors is injected at the input port of the interferometer and then it travels in both arms of the detector thanks to the use of a beam splitter. The length of the Fabry-Perot cavities in the arms is adjusted to be nearly an integer number of half wavelengths of light in order to allow the beam to resonate inside of it. When the beam leaks out of the cavity, it recombines at the beam splitter with the beam coming from the perpendicular arm. Most of the recombined light goes back toward the laser, where it can be collected and sent back to the interferometer through a power recycling mirror, while the remaining light is detected by the photodiode. When a gravitational wave hits the detector the relative position of the test masses gets modified: the length of the two cavities (L_2 and L_1) changes and this translates in a shift of the cavity's resonant frequency with respect to the laser frequency. As a consequence, the phase of the light beams exiting from the two cavities are modified in opposite directions of a quantity proportional to $\Delta L = L_2 - L_1$. This relative phase shift causes a change in the intensity of the recombined light at the photodiode: $I_{pd} \propto \Delta\phi \propto \Delta L \propto h(t)$, where $h(t)$ is the gravitational wave strain.

If the gravitational wave is + polarized (or × polarized) and it is perfectly aligned with the interferometers arms, then the response of the detector is proportional to $h_+(t)$ (or to $h_\times(t)$). More generally however the response of the interferometer will be a linear combination of the two waves polarizations:

$$\frac{\Delta L}{L} = h(t) = F_+(\theta, \phi)h_+(t) + F_\times(\theta, \phi)h_\times(t) \tag{1.23}$$

where $F_+(\theta, \phi)$ and $F_\times(\theta, \phi)$ are called antenna pattern functions and the angles θ and ϕ identify the orientation of the source with respect to the orientation of the interferometer. The combination

$h(t)$ of the two polarizations represents the gravitational wave strain acting on the detector; the time evolution of $h(t)$, $h_+(t)$, and $h_\times(t)$ represents the waveforms.
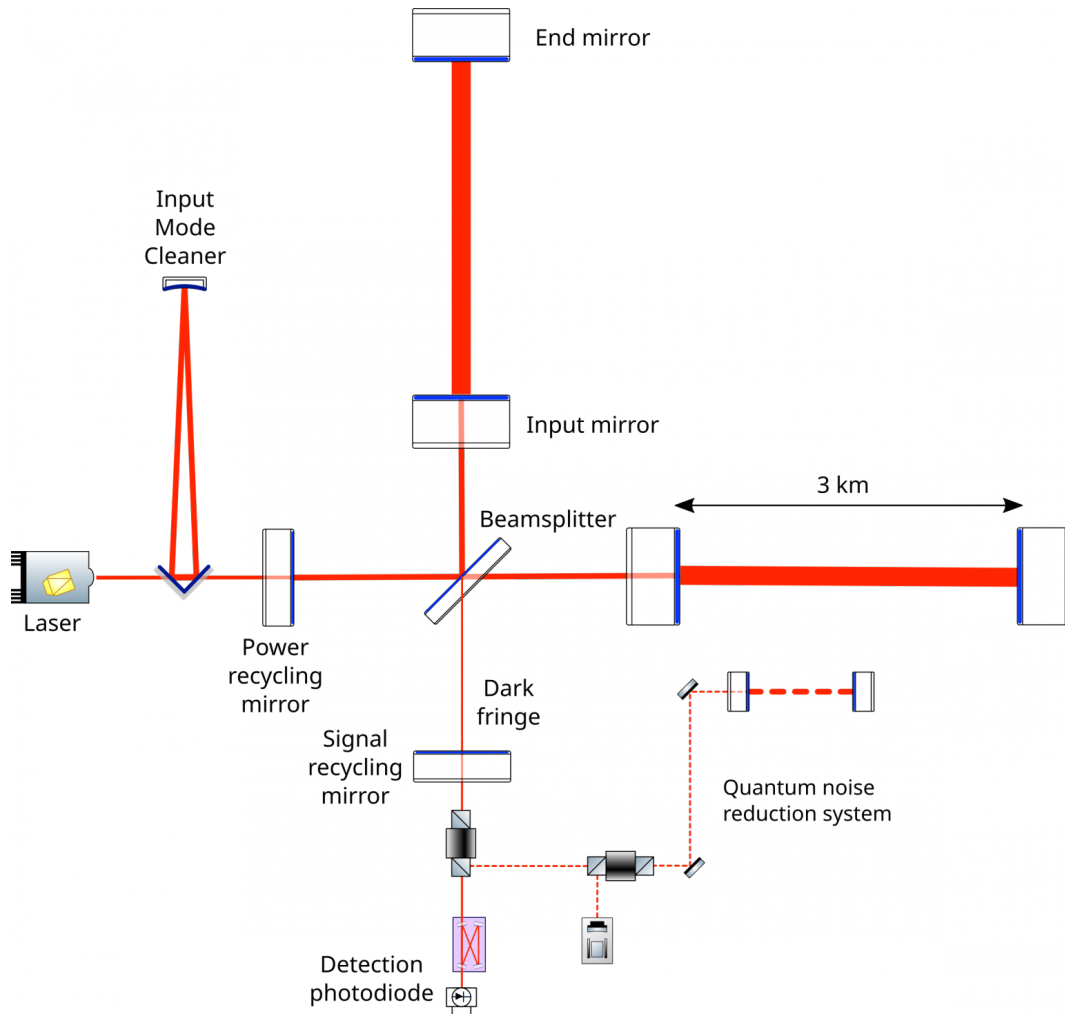

Figure 1.2: Structure of the Virgo gravitational waves interferometer

1.2.2   Sensitivity limit of the interferometers

The scale of sensitivities that ground-based interferometers can achieve is of the order $h \sim 10^{-22}/\sqrt{Hz}$, which corresponds to $1/10000^{th}$ of the width of a proton. Fundamentally it should be possible to build laser interferometry detectors which are limited only by the Heisenberg Uncertainty Principle. Actually this is not really possible due to other effect that must be taken into account. For example, fluctuating gravitational gradients, due to the inhomogeneous mass distribution and movement of the Earth, are a limitation to the sensitivity the interferometer can achieve at low frequencies; this is why experiments to detect sub-Hz gravitational wave signals have to be carried out in space. In general, for ground-based detectors the most important limitations to sensitivity result from the effects of seismic noise, thermal noise associated with the test masses and their suspensions, and quantum noise. The latter is due to the quantum nature of light and it arises as radiation pressure at low frequency, due to momentum transfer from photons to the test masses, and shot noise at high frequency.

The noise budget calculated for the next observation run of Virgo is visible in Figure 1.3.
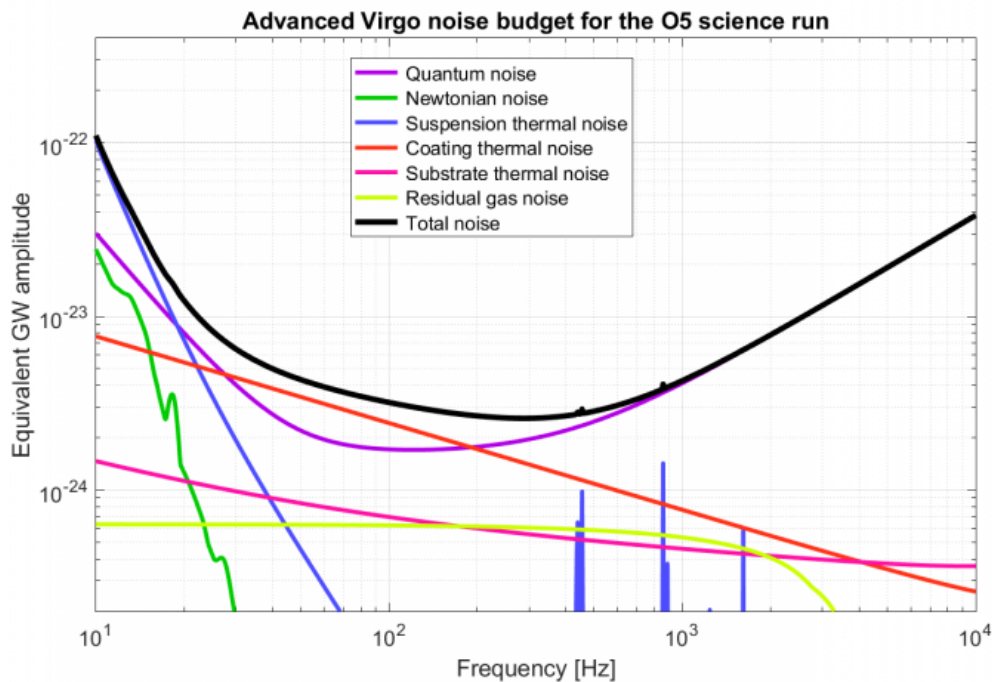
Figure 1.3: Advanced Virgo noise budget for the O5 science run [3]

The main features of the noises affecting the interferometer are outlined more specifically in the following paragraphs:

- **Sismic noise**:
  The ground motion has a big impact on the interferometer performance, and, if it is not attenuated, it would dominate the sensitivity at low frequencies. It originates from ground vibrations caused by various natural and human-induced activities, such as earthquakes, ocean tides, wind, and even nearby traffic. The order of magnitude of ground vibrations is $o(10^{-6}m)$, which is more then 12 orders of magnitude higher then the motion we want to detect; the frequency at which these vibrations occur is in the range $1 - 10$ Hz for human activities and 0.1 Hz for oceanic peaks. This disturbance is an issue even when it occurs in a frequency range that does not coincides whit the detection band: the test masses could be pushed out of their working point, affecting in this way the proper alignment and resonance condition of the interferometer.
  Two different strategies are implemented simultaneously to overcome the problem of vibrations. The active strategy consists in using the so called Internal Seismic Isolation (ISI) system, an instrument able to sense a wide range of environmental vibration frequencies and ground movements. The detected signals are processed in order to generates a net countermotion to cancel all of the external vibrations simultaneously. The passive strategy consists, as mentioned previously, in suspending the test masses to a cascade of pendulums as shown in Figure 1.4. In LIGO, for example, a 4-stagess pendulum is used: the test masses hang at the bottom of this 4-segment pendulum made of 0.4 mm thick fused-silica fibers. The pendulum acts as a passive filter, that attenuates the noise above its resonance frequency as $1/f^2$, thus this configuration is able to absorb almost all movements not completely canceled out by the active system.
  The combination of active and passive vibration damping systems ensure that the interferometer's mirrors are isolated from as much external noise and vibrations as possible.
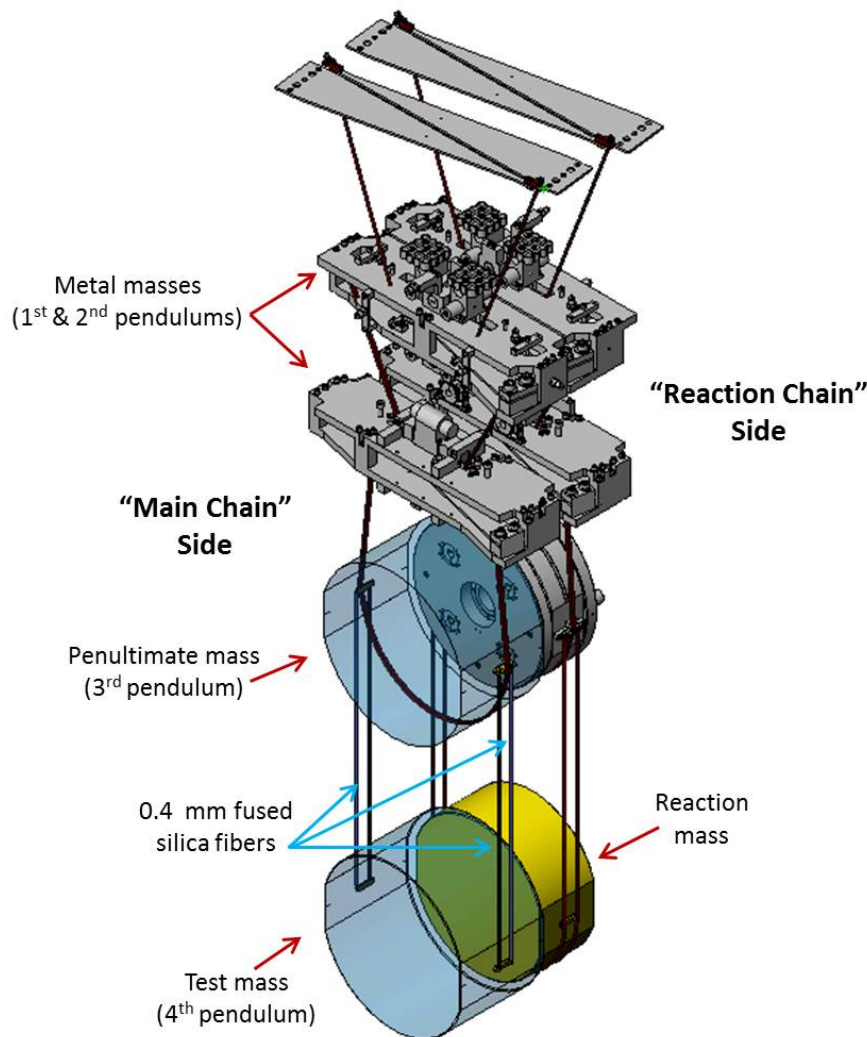
Figure 1.4: LIGO passive vibration damping system: four vibration damping masses are present. [4]

- **Newtonian noise (Gravity gradients)**:
  Gravity gradients refer to stochastic fluctuations of the local gravitational field primarily due to seismic vibrations and infrasound (variations of the atmospheric pressure).
  Gravity gradients can impact gravitational wave detection by inducing small forces on the test masses, forcing them to move slightly as presented in Figure 1.5. If differential forces are applied on different parts of the interferometer the test masses could move in asymmetrical way, causing a distortion of the interferometer's optical paths and disturbing the measurement of the interference pattern. Also, gravity gradients can introduce noise at specific frequencies, which may overlap with the frequency range of astrophysical sources of gravitational waves. This can make it challenging to distinguish genuine gravitational wave signals from noise caused by gravity gradients.
  Also in this case there are active and passive strategies to mitigate this noise. The active strategy consists in deploying a network of sensors to measure ground displacement and atmospheric pressure variations, in order to subsequently model the effect of the measured disturbances on the mirrors and subtract them from the GW signal. The passive strategy consists instead in building the interferometr underground; indeed, as the dominant source

of gravity-gradient noise arises from surface waves on the Earth, then the observed gravity-gradient noise decreases with depth into the Earth. Of course this solution reduces also the impact of the atmospheric pressure variations. For example, the Kamioka Gravitational Wave Detector (KAGRA) in Japan is situated underground in a former mine to minimize noise from environmental factors.
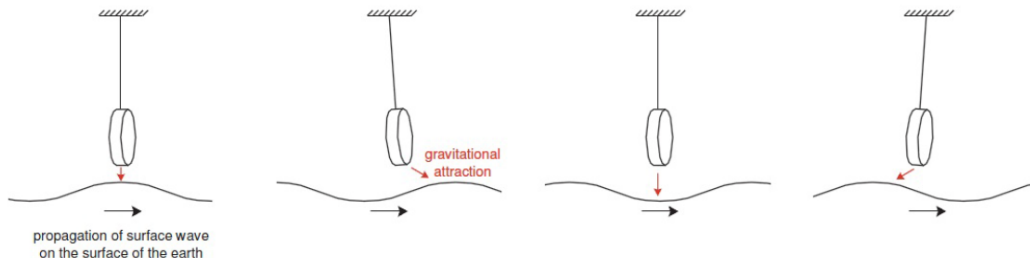

Figure 1.5: Schematic illustration of a fluctuating gravitational force acting on a suspended mass due to the propagation of a surface wave through the ground.

- **Shot noise**:
  Shot noise is a type of fundamental noise that arises in many types of optical and photon-based measurements. It originates from the discrete nature of light, which is composed of individual photons, and the statistical fluctuations in the number of photons arriving at a detector.
  To detect a gravitational wave signal the working point of the interferometer must remain fixed at a certain point of the output interference pattern. In particular, interferometers are operated at, or near, a dark fringe and the detector can be stabilised to this point by sensing with a photodiode any intensity variation at the interferometer output. This error signal is then compared with a reference signal and the result of this operation is comunicated to a transducer able of changing the position of one of the interferometer mirrors. Information about changes in the length of the interferometer arms can then be obtained by monitoring the signal fed back to the transducer.
  For this reason, a limitation to the sensitivity of the optical readout scheme is set by shot noise in the detected photocurrent, which can cause fluctuations of the output power measured by the photodiode. Assuming that the number of photons arriving at the detector follows a Poisson statistic, for which $\Delta N = \sqrt{N}$, the variance of the power can be written as:

$$\Delta P^2 = \frac{\Delta N^2 \hbar^2 \omega_l^2}{T^2} = \frac{P_0 \hbar \omega_l}{T} \tag{1.24}$$

  where ω_l is the laser frequency and P_0 is the input power.
  As photons arrival are uncorrelated, the noise spectrum is expected to be flat and the single sided power spectral density of shot noise can be simply written as:

$$S_P(\omega) = 2P_0 \hbar \omega_l \tag{1.25}$$

From this relation shot noise seems to grow when the power of the beam is increased. However, also the signal increases when the input power is increased. Considering the transfer function of the interferometer and referring this noise to the input it is possible to find that the amplitude spectral density of the strain due to shot noise is proportional to:

$$S_{h,sn}^{1/2} = \frac{1}{L}\sqrt{\frac{4\pi\hbar c \lambda_l}{P_0}} \tag{1.26}$$

where L is the length of the interferometer. Therefore it can be seen that an increase of the input power of the beam can help to reduce the shot noise. It can be calculated that the achievement of the necessary strain sensitivity level would require a laser, operating at a wavelength of 10^{-6} m, to provide a power of about 10^6 W. This is a formidable condition, but fortunately there are a number of techniques which allow a large reduction in this power requirement.

- **Radiation pressure noise**:

  When the effective laser power in the arms of the interferometer is increased, the effect of the fluctuations in the radiation pressure acting on the test masses becomes more and more important.

  Indeed, a beam with input power P_0 exert on the mirror a force equal to $F = 2P/c$. As a consequence, a fluctuation of the beam power is translated in a fluctuation ΔF of this force:

  $$\Delta F = 2\sqrt{\frac{\hbar \omega_l P_0}{c^2 T}} \tag{1.27}$$

  An important consideration is that the beam-splitter divides the photons in the two interferometer arms accordingly to two anti-correlated Poisson distributions. For this reason the contributions of the two arms are summed up and the single sided amplitude spectral density of the radiation pressure turns out to be:

  $$S^{1/2}(\omega) = 4\sqrt{\frac{2\hbar \omega_l P_0}{c^2}} \tag{1.28}$$

  Using the transfer function of a basic interferometer it is possible to refer this noise to the input and calculate the equivalent strain perturbation induced by the radiation pressure as:

  $$S_{h,rp}^{1/2} = \frac{1}{mL\omega^2}\sqrt{\frac{2\hbar \omega_l P_0}{c^2}} \tag{1.29}$$

  where m is the mass of the mirror and ω is the frequency of the detected gravitational wave. Radiation pressure may be a significant limitation at low frequency and is expected to be the dominant noise source in the range between 10 Hz and 50 Hz. The impact of the radiation pressure fluctuations can be reduced by increasing the mass of the mirrors, or by decreasing the laser power at the expense of losing sensitivity at higher frequencies.

1.2.3 The quantum limit

The total quantum noise can be obtained summing the effect of the shot noise and of the radiation pressure [2]:

$$S_h^{1/2}(\omega) = S_{h,sn}^{1/2} + S_{h,rp}^{1/2} \tag{1.30}$$

As explained in the previous paragraph the shot noise contribution is proportional to $P_0^{-1/2}$ while the radiation pressure is proportional to $P_0^{1/2}$. Thus, it is not possible to reduce one contribution without increasing the other: this is a manifestation of the quantum uncertainty principle, due to the fact that we are trying to measure the position of a macroscopic object using photons.
For each gravitational wave frequency ω a certain value of the power P_0 can be chosen to minimize the quantity expressed in Equation 1.30. The corresponding optimal value of $S_h^{1/2}(\omega)$ defines the standard quantum limit (SQL):

$$S_{h,SQL}^{1/2}(\omega) = \frac{1}{\omega L}\sqrt{\frac{8\hbar}{m}} \tag{1.31}$$

The existence of the limiting value $S_{h,SQL}^{1/2}(\omega)$ is a manifestation of the Heisenberg uncertainty principle. However the uncertainty principle does not put a limit on the accuracy of measurements of position, but only on the accuracy of simultaneous measurements of conjugates variables. Thus, it is possible to go beyond the standard quantum limit using, for example, a technique called quantum squeezing, a strategy that consists in injecting squeezed vacuum states through the dark port of the interferometer.

The concept on which this technique is based upon is the fact that in quantum field theory, the electromagnetic field is represented by two non-commuting conjugate operators called quadrature operators. A coherent state (like a laser) has equal uncertainty in both quadrature operators, with the product of uncertainties constrained by the Heisenberg Uncertainty Principle. However, this doesn't prevent the generation of specific states of the electromagnetic field in which the variance of fluctuations in one quadrature is compressed (squeezed) at the expense of the other quadrature. It has been demonstrated that, replacing coherent states with phase-squeezed states improves the interferometer's sensitivity when disturbed by shot noise. Conversely, a squeezed amplitude vacuum state can reduce radiation pressure noise. To achieve noise reduction across the entire spectrum, one employs squeezed states in which the compression level of the two quadrature operators is adjusted based on frequency to effectively counteract the dominant source of quantum noise within a given spectral band. It has been shown that by properly preparing these states, it's even possible to surpass the standard quantum limit, albeit only within a certain bandwidth.

1.2.4   Thermal noise

Thermal noise is due to thermally induced vibrations both in the mirrors and in the suspensions. Its effect can be computed using the fluctuation-dissipation theorem [5].

Indeed, the equation of motion for a linear system subject to a force F can be written in the form:

$$\tilde{F}(\omega) = -i\omega Z(\omega)\tilde{x}(\omega) \tag{1.32}$$

where $Z(\omega)$ is the impedance of the system.

The fluctuation dissipation theorem states that the single sided power spectral density of the force responsible for thermal fluctuations $S_F(\omega)$ is related to the real part of the impedance as:

$$S_F(\omega) = 4k_B T \,\Re(Z(\omega)) \tag{1.33}$$

At this point the displacement spectral density is given by:

$$x(\omega) = \frac{1}{\omega|Z(\omega)|}\sqrt{4k_B T \,\Re(Z(\omega))} \tag{1.34}$$

For a complex extended object the impedance associated to a normal mode with frequency ω_0 can be modeled as:

$$Z(\omega) = -\frac{im}{\omega}[\omega^2 - \omega_0^2 + i\omega^2\phi(\omega)] \tag{1.35}$$

where the dimensionless function $\phi(\omega)$ is called the loss angle.

With regards to the effect induced by thermal noise in the suspension of the test masses there can be:

- Pendulum thermal fluctuations: these thermal fluctuations induce a swing motion in the suspensions, that translates in a horizontal displacement of the mirrors. This effect is dominant between few Hz and 50 Hz;

- Vertical fluctuations: due to the Earth curvature and to the significant length of the interferometer's arms, a vertical motion of a mirror can result in a non-negligible vertical-horizontal displacement coupling;

- Violin modes: they are fluctuations of the normal modes of the wires and they result in a set of spikes between few hundred Hz and few kHz (see Figure 1.3).

Of course there are thermal fluctuations also within the test masses themselves and these are mainly due to Brownian motion of the mirrors. Indeed, the atoms of a mirror at finite temperature T have a Brownian motion due to their kinetic energy, which give rise to mirror thermal noise. At present, this is the dominant noise between a few tens and a few hundred Hz.

As seen in the previous paragraph, in order to reduce shot noise and achieve the sensitivity needed to detect gravitational waves, a very high optical power is required to circulate inside the interferometer. This complicates the characteristics that the mirrors have to provide in order to guarantee low optical losses, that in this case will be mainly due to absorption and scattering. In particular, the mirror reflectivity has to be grater then 99.9 % with an absorption level lower then 0.5 ppm and scattering losses lower then 2 ppm. The only type of mirrors that can ensure these properties are dielectric Bragg mirrors made of multi-layers coatings deposited on a substrate (see Figure 1.6).

Also in this case, when the system is at thermal equilibrium, the fluctuations-dissipation theorem allows to relate the mechanical losses of the material to its thermal fluctuations and the Brownian noise affecting the mirrors can be written as [10]:

$$S_{th}(f) = \frac{k_B T}{\pi^2 f} \frac{d\phi(f)}{w^2 Y_S} \left(\frac{Y_C}{Y_S} + \frac{Y_S}{Y_C} \right) \tag{1.36}$$

where Y_S and Y_C are the Young modulus of the substrate and of the coating respectively, d is the coating thickness and w is the beam size. The factor $\phi(f)$ is the mechanical loss angle, which describes the phase lag between the stress applied to a material and its strain response; it is defined as [8]:

$$\phi(f_0) = \frac{\Delta E}{2\pi E_{TOT}} = \frac{\Delta f}{f_0} = \frac{1}{Q} \tag{1.37}$$

with ΔE the energy dissipated during one oscillation and E_{TOT} the total energy contained in the oscillating system.

Some of the strategies to reduce thermal noise are: the lowering of the temperature at which GW interferometers operate, the reduction of the multilayer stack thickness and the employment of materials with lower mechanical dissipations.

Up to now the mirror coatings are constituted by alternating layers of amorphous silica SiO_2, with index of refraction $n = 1.45$ and tantalum pentoxide with $n = 2.10$. Thus, silica is the low index of refraction material while tantala is the high index of refraction material. The optical losses of this coating is of the order of 1 ppm (at the wavelength currently used $\lambda = 1064$ nm). The mechanical losses are dominated by the tantala layers that are characterized by a loss angle of about 4×10^{-4}, while the mechanical dissipations of silica are one order of magnitude lower (around 5×10^{-5}). These considerations point out the importance of manufacturing high refractive index materials with lower mechanical loss angles.
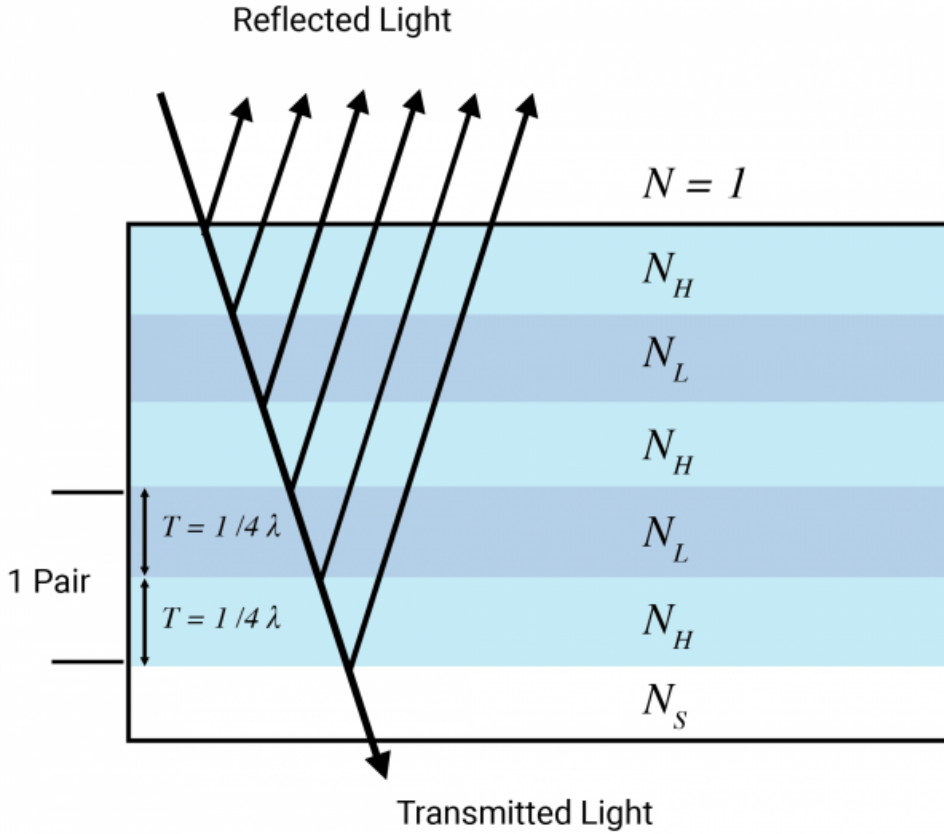
Figure 1.6: High reflectivity dielectric mirrors are made of alternating layers of high and low index of refraction. The thickness of each layer is equal to $\lambda/4$.

1.2.5 Current methods for studying coating thermal noise

Standard methods for the characterization of the coatings generally require them to be deposited on a substrate. The substrates used for the deposition are fused silica or silicon wavers when studying optical losses, while fused silica disk resonators are employed when the mechanical properties are under investigation [7].

Regarding the optical characterization, different techniques such as transmission spectroscopy or spectroscopic ellipsometry can be used to measure the refractive index and the thickness of different coatings. Very small optical absorption losses can be evaluated through photo-thermal deflection, while scattering losses can be measured by appropriate optical setups.

The mechanical characterization consists instead in measuring the mass, the mass density and the coating mechanical losses. These losses can be measured applying the ring down method to the resonating disk on which the coating is deposited and measuring the ring down time of its vibrational modes. More specifically the loss angle of the deposited coating can be calculated starting from the mode frequency and the measured ring down time as:

$$\phi_k^{C+S} = \pi(f_k\tau_k)^{-1} \tag{1.38}$$

where k indicates the mode number.

The same measurement is repeated in the case of the substrate alone to obtain the loss angle of the substrate and then to calculate the loss of the coating alone as:

$$\phi_k^C = \frac{\left[\phi_k^{C+S} + (D_k - 1)\phi_k^S\right]}{D_k} \tag{1.39}$$

Where D_k is the dilution factor, defined as the ratio between the elastic energy of the coating and the elastic energy of the system formed by coating and the substrate together. This factor depends on the frequency of the resonant mode considered.

It is evident that this method of measurement presents different complications due to the fact that to obtain the coating mechanical dissipation a simple subtraction is not enough, but instead it is necessary to take into account different corrections that are complex to model. Indeed, the dilution factor cannot be measured directly and it has to be estimated using the finite elements method (FEM). In the same way, the thermoelastic losses, i.e. the energy dissipated inside the mirror due to the different thermoelastic properties of coating and substrate, are difficult to model at room temperature and unknown at cryogenic temperature.

The impossibility to perform a direct measurement of the mechanical losses of the coating without including the substrate effect, along with the need to implement different measurement setups to measure optical and mechanical properties is therefore pushing the development of new experimental setups to measure their properties.

Chapter 2

Fundamentals of Gaussian optics

2.1 The Helmholtz equation

The propagation of an electromagnetic field through vacuum or in a homogeneous isotropic medium (in this case c is substituted with $v = c/n$) is described by the electromagnetic wave equation that can be derived from Maxwell's equations:

$$\left(\nabla^2 - \frac{1}{c^2} \frac{\partial^2}{\partial t^2} \right) u(\vec{r}, t) = 0 \tag{2.1}$$

The fact that this equation is linear implies that if $u_1(\vec{r}, t)$ and $u_2(\vec{r}, t)$ are solutions of the equation, then also $a\, u_1(\vec{r}, t) + b\, u_2(\vec{r}, t)$ is a possible solution.
Monochromatic waves are the simplest solutions to the wave equations and they can be written as the product of a function of the only position and an harmonic function of time:

$$u(\vec{r}, t) = a(\vec{r}) \cos\left(2\pi\nu t + \varphi(\vec{r})\right) \tag{2.2}$$

Using this formalism however the wave function is not completely factorized. For this reason monochromatic waves are usually written in complex form as:

$$U(\vec{r}, t) = a(\vec{r}) e^{i\varphi(\vec{r})} \times e^{2\pi i \nu t} = U(\vec{r}) \times e^{2\pi i \nu t} \tag{2.3}$$

In this way the wave function is given by a complex amplitude depending only on the position and a second term depending only on time and oscillating at a precise frequency ν. From the linearity of the waves equation it is possible to show that also the complex wave function is a possible solution of Equation 2.1. This representation of the electromagnetic field is advantageous also to calculate the intensity of the field, which is completely determined by the complex amplitude as the time oscillating part is averaged to zero when integrating on periods much longer then $1/\nu$:

$$I(\vec{r}) = |u(\vec{r}, t)|^2 = |U(\vec{r})|^2 \tag{2.4}$$

The physical electromagnetic field is then described by the real part of Equation 2.3:

$$u(\vec{r}, t) = \Re[U(\vec{r}, t)] \tag{2.5}$$

For monochromatic waves the angular frequency $\omega = 2\pi\nu$ and the wave vector $\vec{k}$ must be related by the dispersion relation:

$$k = |\vec{k}| = \frac{\omega}{c} = \frac{2\pi}{\lambda} \tag{2.6}$$

By inserting Equation 2.3 into the wave equation one obtains the time independent Helmoholtz equation:

$$\left(\nabla^2 + k^2\right)\vec{U}(\vec{r}) = 0 \tag{2.7}$$

The simplest solutions of the Helmholtz equation in an homogeneous medium are the planar waves and the spherical waves.

Planar waves are obtained solving the Helmholtz equation in Cartesian coordinates and the complex amplitude has the simple form:

$$U(\vec{r}) = Ae^{-i\vec{k}\cdot\vec{r}} \tag{2.8}$$

where A is a complex constant. In this case the wavefronts are perpendicular to the wave vector $\vec{k}$ and the intensity is constant.

If on the contrary the Helmholtz equation is solved using spherical coordinates, then spherical waves are obtained. This time the complex amplitude is written as:

$$U(\vec{r}) = \frac{A}{r}e^{-i\vec{k}\cdot\vec{r}} \tag{2.9}$$

where as before A is a complex constant, but in this case the intensity decreases with the square of the distance $\vec{r}$ from the source.

For our purposes it is interesting to notice that plane waves and spherical waves have different characteristics: the first one is completely delocalized but it propagates in a specific direction, the second one propagates in all directions, but it originates from a completely localized source.

In the next paragraph the description of an optical field that is confined in space while it propagates in a well-defined direction will be treated.

2.2   The Gaussian principal mode

For the case of interest of this thesis I will focus on the characteristics of the electromagnetic beams produced by lasers, that can be well described as Gaussian beams. The Gaussian beam corresponds to the fundamental mode of a spherical mirror resonator. Its complex amplitude is given by [11]:

$$E(z,\rho) = \frac{A_0}{k(z - iz_0)}\exp\left(i\frac{k\rho^2}{2(z - iz_0)}\right)e^{ikz} \tag{2.10}$$

where, to make more evident the properties of the fundamental TEM_{00} it is useful to introduce two quantities, $R(z)$ and $w(z)$, through the relation:

$$\frac{1}{z - iz_0} = \frac{z + iz_0}{z^2 + z_0^2} = \frac{1}{R(z)} + \frac{2i}{kw^2(z)} \tag{2.11}$$

Then the Fresnel factor can be decomposed into one real and one imaginary part:

$$\exp\left(i\frac{k\rho^2}{2(z - iz_0)}\right) = \exp\left(i\frac{k\rho^2}{2R(z)}\right)\exp\left(-\frac{\rho^2}{\omega^2(z)}\right) \tag{2.12}$$

where the complex phase describes the curvature of the wavefront, while the real factor represents the envelope of the beam profile.

Using Equation 2.11 and Equation 2.12 the final expression of the Gaussian beam is obtained:

$$E(r,z) = E_0\frac{w_0}{w(z)}\exp\left(-\frac{r^2}{w(z)^2}\right)\exp\left[-i\left(\frac{kr^2}{2R(z)} + kz - \psi(z)\right)\right] \tag{2.13}$$

where $E_0 = E(0,0)$ is the field amplitude in the origin, r is the radial distance from the beam axis, k is the wave number and z is the axial distance from the beam waist.
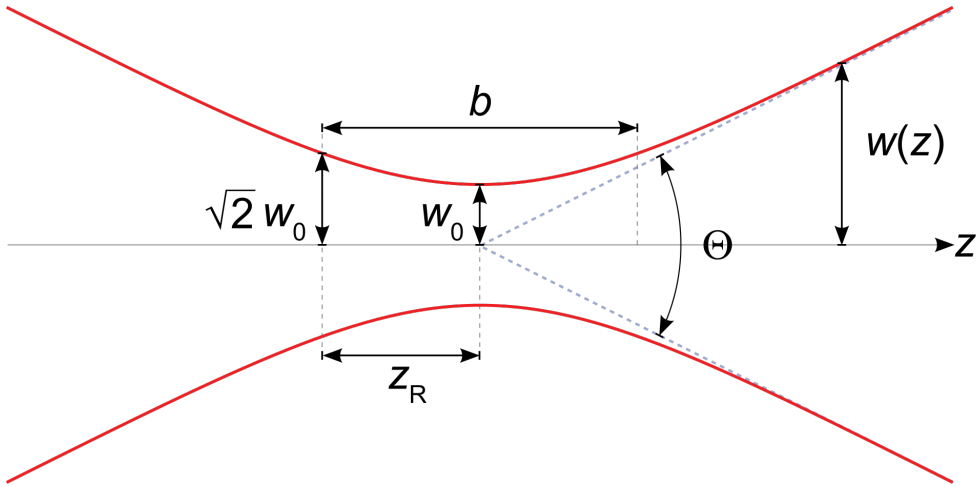

Figure 2.1: Scheme of a Gaussian beam .

There are certain parameters used to describe specific characteristics of the beam (visualized also in Figure 2.1):

- **Rayleigh parameter**
  It is defined as the distance from the waist where the cross-sectional area of the beam has increased by a factor of $\sqrt{2}$ from its minimum value. At the Rayleigh range, the beam diameter is larger than at the waist, and beyond this distance, the beam continues to diverge.
  The Rayleigh range is directly proportional to the square of the beam's initial waist size and inversely proportional to the wavelength. Mathematically:

$$z_R = \frac{\pi w_0^2}{\lambda} \tag{2.14}$$

- **Beam waist**
  It is indicated as w_0 and it is the parameter defining the dimension of the beam radius at $z = 0$:

$$w_0^2 = \frac{\lambda z_0}{\pi} \tag{2.15}$$

If the beam propagates in a medium then λ must be substituted with λ/n.

- **Beam radius**
  This parameter defines the beam radius at a distance z from the focus:

$$w(z) = w_0 \sqrt{1 + \left(\frac{z}{z_0}\right)^2} \tag{2.16}$$

Within the Rayleigh region the beam radius remains approximately constant, while in the far field it increases linearly as $w(z) \simeq w_0 z / z_0$.

- **Wavefront curvature**
  It refers to the radius of the wavefront of the beam and it measures how the beam converges or diverges at a particular point along its propagation path. The radius of curvature varies as the beam propagates through space along z as:

$$R(z) = z\left(1 + \left(\frac{z_R^2}{z^2}\right)\right) \tag{2.17}$$

  At the beam waist ($z = 0$), the radius of curvature is infinite, indicating that the beam is at its narrowest point, and its wavefront is essentially flat. The approximation $R(z) \to \infty$ holds within the region $z \ll z_R$. The largest curvature (or the smaller radius) occurs at $z = z_R$, where $R(z_R) = 2z_R$. In the far field region $z \gg z_R$ one can consider $R(z) \simeq z$.

- **Divergence**
  This parameter quantifies how quickly the beam radius increases with distance from the focus. It is inversely proportional to the initial beam radius w_0:

$$\theta = \frac{\lambda}{\pi n w_0} \tag{2.18}$$

  A smaller divergence angle indicates that the beam spreads out more slowly and remains more tightly focused over long distances.

- **Gouy phase**
  It represents a small deviation from the linear phase evolution of the planar wave and it is given by:

$$\psi(z) = \arctan\left(\frac{z}{z_R}\right) \tag{2.19}$$

  in the range $-\pi/2 \leq \psi(z) \leq \pi/2$. Half of this phase is collected within the Rayleigh range.

- **Intensity profile**
  Computing the intensity profile of the beam in the plane perpendicular to the propagation direction one obtain the expected Gaussian distribution:

$$I(r, z) = \frac{c\epsilon_0}{2} E E^* = \frac{c\epsilon_0}{2} |E_0|^2 \left(\frac{w_0}{w(z)}\right)^2 e^{-2r^2/w^2(z)} \tag{2.20}$$

  Thus for every position z along the propagation axis, the intensity has the highest value at $r = 0$ and then it gradually decreases towards the edges. The peak value is:

$$I(0, z) = \frac{c\epsilon_0}{2} |E_0|^2 \left(\frac{w_0}{w(z)}\right)^2 \tag{2.21}$$

  Differently, along the z axis the intensity follows a Lorentzian distribution:

$$I(0, z) = \frac{I_0}{1 + (z/z_R)^2} \tag{2.22}$$

  and it varies from its maximum value $I(0,0) = (c\epsilon_0/2)|E_0|^2$ to half of this value at the limit of the Rayleigh region $z = z_R$.
  The total power contained in the Gaussian beam can be computed as:

$$P = 2\pi \int_0^\infty I(r,z)\, r dr = \pi w_0^2 E_0^2 \tag{2.23}$$

2.3   The higher order modes

The Gaussian beam described so far is the lowest order solution to the paraxial Helmholtz equation. This last equation is a simplification of the Helmoltz equation that can be use to describe the propagation of optical waves in the paraxial approximation.

Mathematically, the paraxial Helmholtz equation is obtained supposing that the wave amplitude varies very slowly along the z direction, therefore:

$$\frac{\partial^2 A}{\partial x^2} + \frac{\partial^2 A}{\partial y^2} - 2ik\frac{\partial A}{\partial z} = 0 \tag{2.24}$$

The TEM_{00} is only one of the solution of the paraxial Helmholtz equation. A more general and complete orthogonal set of wavefront solutions are the Hermite-Gaussian (HG) modes which include beams with non-Gaussian intensity distributions.
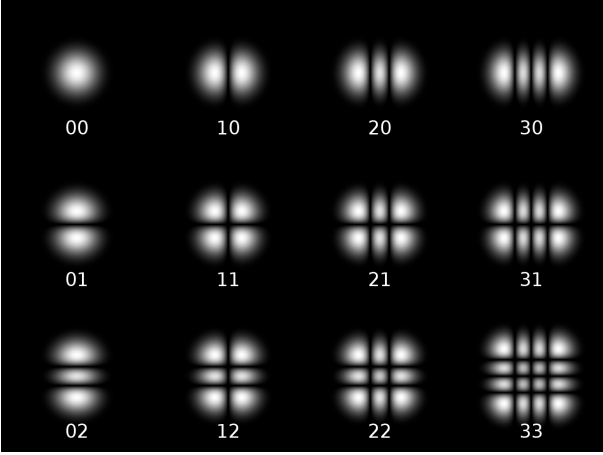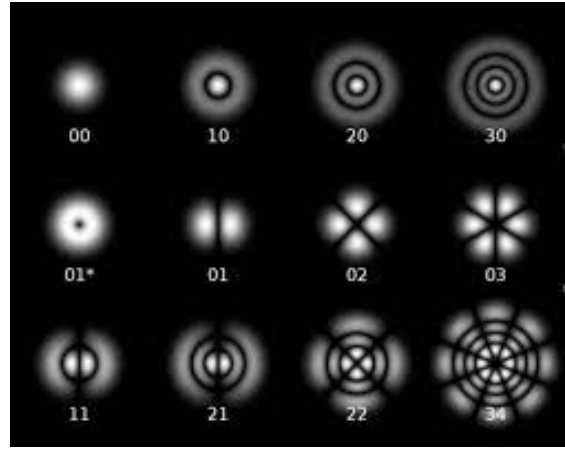

Figure 2.2: Hermite-Gaussian modes.

Figure 2.3: Laguerre-Gaussian modes.

This set of solution is represented using Cartesian coordinates:

$$
\begin{aligned}
E_{mn}(x,y,z) =& E_0 H_m\left(\frac{\sqrt{2}x}{w(z)}\right) H_n\left(\frac{\sqrt{2}y}{w(z)}\right) \frac{w_0}{w(z)} \\
&\times \exp\left(-\frac{r^2}{w(z)^2}\right) \exp\left[-i\left(\frac{kr^2}{2R(z)} + kz - (m+n+1)\psi(z)\right)\right]
\end{aligned} \tag{2.25}
$$

All the other sets of solutions could be defined as a composition of the HG modes. For example, a solution of the paraxial Helmholtz equation in cylindrical coordinates defines the Laguerre-Gauss (LG) modes, whose normalized expression is:

$$
\begin{aligned}
U_{p,l}(r,\phi,z) =& \frac{Ap,l}{w(z)}\left(\frac{\sqrt{2}r}{w(z)}\right)^{|l|} L_p^{|l|}\left(\frac{2r^2}{w^2(z)}\right) \\
&\times \exp\left(-\frac{r^2}{w(z)^2}\right) \exp\left[-i\left(\frac{kr^2}{2R(z)} + kz + l\phi - (|l|+2p)\psi(z)\right)\right]
\end{aligned} \tag{2.26}
$$

where L_p^l are the generalized Laguerre polynomials and $Ap, l = \sqrt{\frac{2p!}{\pi(|l|+p)!}}$ is a normalization constant.

In both cases the lowest order mode corresponds to the TEM00.

2.4 The ABCD method for Gaussian beams

The ABCD rule is a very useful method to analyze how Gaussian laser beams propagate through optical systems. It is an extension of the ABCD rule known from ray optics and it allows to calculate how the size and divergence of the beam change as it interacts with various optical elements like lenses and mirrors.

According to this method, when a light ray interacts with an optical element, its parameters are transformed linearly according to the relation:

$$\begin{pmatrix} r_2 \\ \alpha_2 \end{pmatrix} = \mathbf{M} \begin{pmatrix} r_1 \\ \alpha_1 \end{pmatrix} = \begin{pmatrix} A & B \\ C & D \end{pmatrix} \begin{pmatrix} r_1 \\ \alpha_1 \end{pmatrix} \tag{2.27}$$

where (r_i, α_i) are respectively the distance from the z axis and the angle between the ray and the axis as indicated in Figure 2.4.
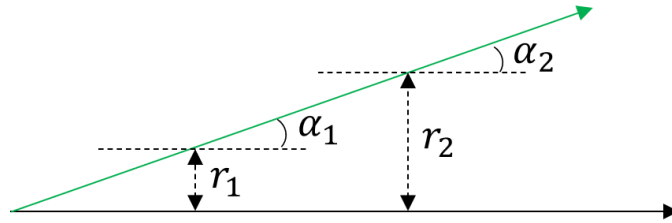

Figure 2.4: Variables describing an optical ray

The effect of every optical element can be represented using a different ABCD matrix. The most common situations are the following:

- **Free space propagation**:
  For a ray propagating in a straight line through empty space the transfer matrix is:

$$\mathbf{M} = \begin{pmatrix} 1 & d \\ 0 & 1 \end{pmatrix} \tag{2.28}$$

- **Planar surface refraction**:
  The refraction at an interface between two mediums with refractive indices n_1 and n_2 is defined by the Snell's law. When it is possible to use a paraxial approximation $sin\theta \sim \theta$ the Snell's law becomes $n_1\theta_1 = n_2\theta_2$ and the matrix can be written as:

$$\mathbf{M} = \begin{pmatrix} 1 & 0 \\ 0 & \frac{n_1}{n_2} \end{pmatrix} \tag{2.29}$$

- **Curved surface refraction:**

  In this case Snell's law in paraxial approximation is applied to a ray impinging on a spherical surface at a distance r_1 from the optical axis and with an angle of incidence $\theta_1 = \alpha_1 + \phi$ with
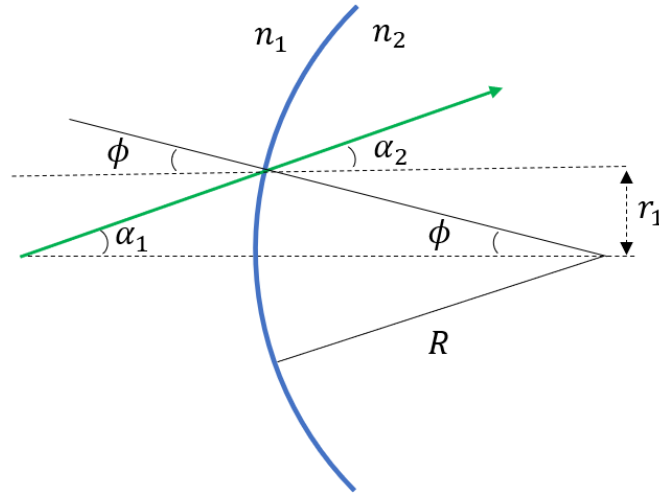
Figure 2.5: Scheme of the refraction from a curved surface

respect to the normal to the surface, with $\phi = \frac{r_1}{R}$. Considering that $r_1 = r_2$ and $n_1\theta_1 = n_2\theta_2$ it is possible to calculate:

$$\mathbf{M} = \begin{pmatrix} 1 & 0 \\ \frac{1}{R}\frac{n_1-n_2}{n_2} & \frac{n_1}{n_2} \end{pmatrix} \tag{2.30}$$

- **Thin lenses**:
  The matrix for the propagation through a lens can be written as the product between the three matrices representing the curved input surface R_{in}, the transmission through the lens medium of length d and the curved output surface R_{out}. For thin lenses this result can be simplified considering the approximation $\frac{d}{R_{in}}, \frac{d}{R_{out}} \ll 1$. In this case one obtain:

$$\mathbf{M} = \begin{pmatrix} 1 & 0 \\ \frac{1}{f} & 1 \end{pmatrix} \tag{2.31}$$

where f is the lens focus and it is defined as:

$$\frac{1}{f} = -(n-1)\left(\frac{1}{R_{out}} - \frac{1}{R_{in}} \right) \tag{2.32}$$

The above matrices were obtained starting from ray optics concept, however the parameters of the Gaussian beam can be modified correctly exploiting the same linear transformations. Indeed, at every position z along the propagation direction the Gaussian beam is completely characterized by the parameters (w_0, z_0). Equivalently, it can also be characterized knowing the complex parameter $q(z) = z - iz_R$; it is precisely to this parameter that the transfer matrices are applied:

$$q_1 = \mathbf{M} \otimes q_0 = \frac{Aq_0 + B}{Cq_0 + D} \tag{2.33}$$

where q_0 is the complex parameter of the initial beam and q_1 is the complex parameter of the final beam. Of course this method can be applied multiple times simply exploiting the matrix product:

$$q_1 = \mathbf{M}_2 \otimes (\mathbf{M}_1 \otimes q_0) \tag{2.34}$$

Chapter 3

Optical resonators

3.1 Elementary properties of an optical resonator

An optical resonator (or cavity) is a set of mirrors arranged in a way to trap light at specific resonant frequencies.
Optical cavities can be divided in two groups:

- Standing wave cavities: they are also called Fabry-Perot interferometers and they are obtained by placing two flat mirrors facing each other at a certain distance, in this way the interference of the two counter-propagating waves creates a standing wave. The light reflected from the cavity travels straight toward the external source.

- Traveling wave cavities: the cavity is formed by more then two mirrors and light can travel in the cavity in both directions. In this case there is no light reflected back toward the external source.

In this section the basic physical properties of resonant cavities will be defined.

3.1.1 Properties of an optical cavity

Considering the easiest situation, a Fabry-Perot interferometer is typically made by two high-reflective mirrors placed at a distance L [11]. When an electric field impinges on the first mirror a certain percentage of the light penetrates inside the cavity and starts to circulate in it; in the same way a certain amount of radiation is transmitted by the second mirror while the rest is reflected back toward the input mirror. Between the two mirrors, the resulting electromagnetic field is given by the superposition of all the reflected waves. Due to interference, the only waves that do not cancel each other out are those for which the optical path length of a complete round-trip inside the cavity is an integer multiple q of the wavelength λ. In this way a standing wave develops between the two mirrors and the intensity of the electromagnetic radiation grows inside the cavity. The condition to have constructive interference is therefore:

$$q\lambda = 2L \tag{3.1}$$

It is possible to describe the response signal of a Fabry-Perot cavity assuming the fields to be stationary and related to the initial field injected into the cavity. Indicating the input field's amplitude as E_{in}, the field E_c circulating inside the cavity can be written as:

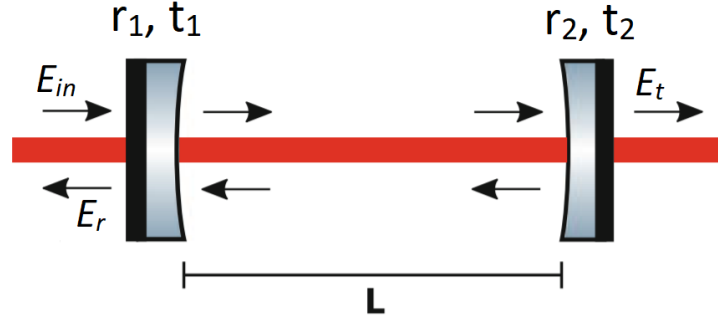$$E_c = it_1 E_{in} + g_{rt}(\omega)E_c \tag{3.2}$$

Figure 3.1: Scheme of a Fabry-Perot interferometer.

where $g_{rt}(\omega)$ is the so called complex round trip gain, a parameter describing the amplitude gain of the cavity after one round trip.

Indeed, a real cavity is characterized by a certain amount of optical losses due to scattering and absorption that can be quantified using the absorption coefficient α_0. Then the amplitude attenuation after one round trip corresponds to $e^{-2\alpha_0 L}$. Thus, the round trip gain is equal to:

$$g_{rt}(\omega) = r_1 r_2 \times \exp\left[-2\alpha_0 L - i\frac{2\omega L}{c}\right] \tag{3.3}$$

where r_1 and r_2 are the mirrors reflection coefficients. In a passive optical cavity $|g_{rt}(\omega)| < 1$. The exponential factor $2\omega L/c = 2kL$ corresponds to the phase shift acquired in one round trip. This result can be extended to the case of a travelling wave cavity simply using the perimeter length of the cavity (instead of twice the distance L between the two mirrors) and adding the reflectivity of the additional mirrors.

At this point the circulating field can be written as:

$$E_c = \frac{it_1}{1 - r_1 r_2 \exp\left[-2\alpha_0 L - i2\omega L/c\right]} E_{in} \tag{3.4}$$

It is now possible to notice that the condition to have a resonance behaviour is given by:

$$\frac{2\omega L}{c} = q \times 2\pi \tag{3.5}$$

Which means that the resonant frequencies (or cavity axial modes) are:

$$\omega = \omega_q = \frac{q\pi c}{L} \tag{3.6}$$

The computation of the field intensity allows to study some interesting properties of the optical cavity. At resonance, the circulating field intensity I_c is given by:

$$\left.\frac{I_c}{I_{in}}\right|_{\omega=\omega_q} = \frac{t_i^2}{\left[1 - r_1 r_2 e^{-2\alpha_0 L}\right]} \tag{3.7}$$

From Figure 3.2 it can be noticed that, when the resonance condition is satisfied, the intensity of the field E_c that builds up inside the cavity can become much bigger then the intensity of the input filed E_{in}. This can happen in two cases:

- if r_1, $r_2 \sim 1$ and $\alpha_0 << 1$: in this case the denominator gets very close to zero;
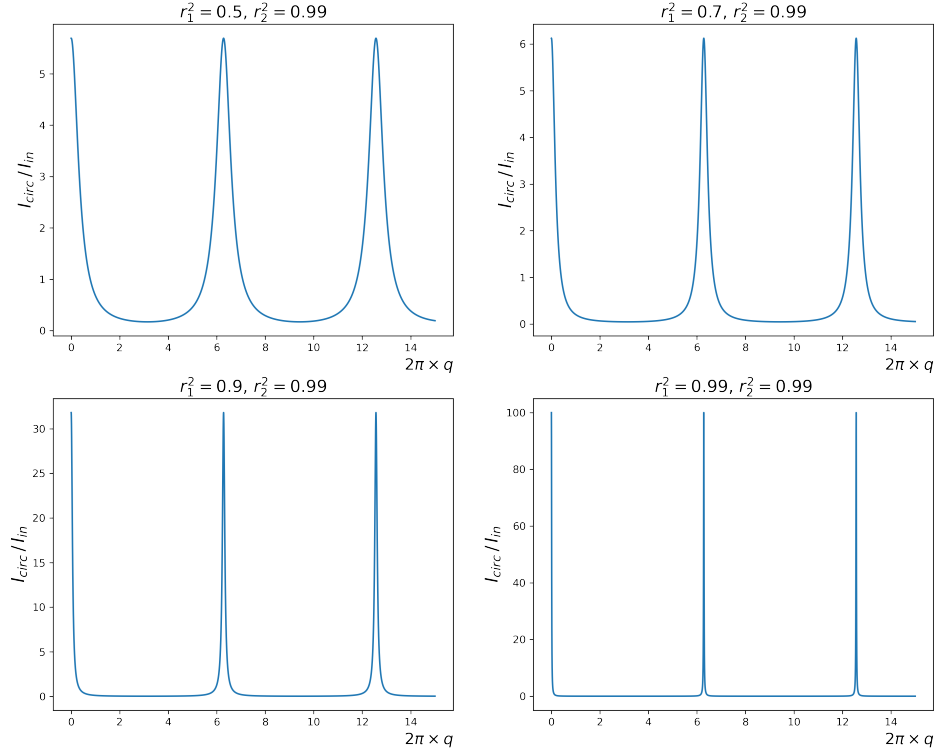
29

Figure 3.2: These plots show how the intensity of the field circulating inside the cavity at resonance changes according to the value of the input mirror reflectivity.

- if the denominator is much smaller then t_1: in this case $I_c >> I_{in}$;

Using the same arguments the field transmitted through the cavity can be written as:

$$E_t = it_2 \exp\left[-\alpha_0 L - i\frac{\omega L}{c}\right] E_c \qquad (3.8)$$

And the normalized amplitude is:

$$\frac{E_t}{E_{in}} = \frac{-t_1 t_2 \exp\left[-\alpha_0 L - i\frac{\omega L}{c}\right]}{1 - r_1 r_2 \exp\left[-2\alpha_0 L - i\frac{2\omega L}{c}\right]} \qquad (3.9)$$

This can be rewritten in a more compact way as a function of the complex round trip gain:

$$\frac{E_t}{E_{in}} = -\frac{t_1 t_2}{\sqrt{r_1 r_2}} \frac{\sqrt{g_{rt}(\omega)}}{1 - g_{rt}(\omega)} \qquad (3.10)$$

The intensity of the transmitted field at resonance is given by the following equation:

$$\left.\frac{I_t}{I_{in}}\right|_{\omega=\omega_q} = \frac{t_1^2 t_2^2}{|1 - g_{rt(\omega)}|^2} \qquad (3.11)$$

The reflected beam E_r is given instead by the superposition of two fields: the one promptly reflected by the input mirror and the one circulating inside the cavity and leaking out from the input mirror. E_r is therefore written as:

$$E_r = r_1 E_{in} + it_1 \frac{g_{rt}(\omega)}{r_1} E_c \tag{3.12}$$

As already done before the normalized amplitude of the reflected field can be obtained substituting the expression for the circulating field:

$$\frac{E_r}{E_{in}} = r_1 - \frac{t_1^2}{r_1} \frac{g_{rt(\omega)}}{1 - g_{rt(\omega)}} \tag{3.13}$$

Using now the relation $r_1^2 + t_1^2 = 1$ it is easy to find:

$$\frac{E_r}{E_{in}} = \frac{1}{r_1} \times \frac{r_1^2 - g_{rt}(\omega)}{1 - g_{rt}(\omega)} \tag{3.14}$$

From this relation it is possible to see that the reflected field can go to zero at resonance if:

$$r_1^2 = g_{rt}(\omega = \omega_q) = r_1 r_2 e^{-2\alpha_0 L} \tag{3.15}$$

In this case the cavity is said to be impedance matched.
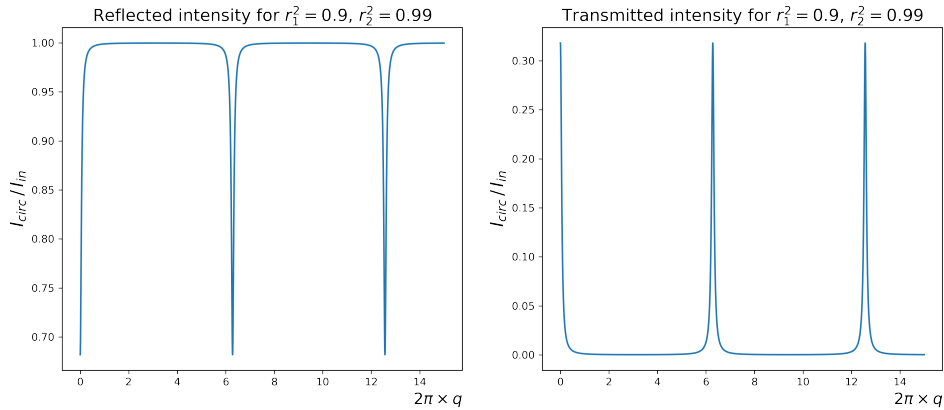The intensity behaviour of the fields reflected and transmitted by the cavity is visible in Figure 3.3

Figure 3.3: These plots show the intensities of the fields reflected and transmitted by the cavity.

3.1.2   The finesse of an optical cavity

From Figure 3.3 it is possible to understand that the Fabry-Perot interferometer generates a periodic series of transmission lines as a function of the incident radiation frequency $\omega = ck$. The distance between adjacent resonant frequencies is called Free Spectral Range (FSR):

$$FSR \equiv \nu_{q+1} - \nu_q = \frac{c}{2L} \tag{3.16}$$

To understand if an optical cavity has a resolution that allows to separate the peaks corresponding to different resonant frequencies, it is necessary to determine the width of the trasmission maxima. This width can be computed finding the frequency ω_{HM} for which:

$$I_{t,HM}(\omega_{HM}) = \frac{I_{t,max}}{2} \tag{3.17}$$

where $I_{t,max}$ is the intensity transmitted through the cavity at resonance and $I_{t,HM}(\omega_{HM})$ is the intensity transmitted through the cavity when the field has a frequency $\omega = \omega_{HM}$.
Rewriting this expression in terms of the complex round trip gain one obtain the equation:

$$\frac{1}{2} = \frac{I_{t,HM}(\omega_{HM})}{I_{t,max}} = \frac{|1 - g_{rt}|^2}{|1 - g_{rt}(\omega_{HM})|^2} \tag{3.18}$$

The solution of this equation is the value of the frequency ω_{HM} and then the full width at half maximum is defined as:

$$\Delta\omega_{HM} \equiv 2\omega_{HM} = \frac{4c}{p}\arcsin\left(\frac{1 - g_{rt}}{2\sqrt{g_{rt}}}\right) \simeq 2\,FSR\,\frac{1 - g_{rt}}{2\sqrt{g_{rt}}} \tag{3.19}$$

where g_{rt} is calculated at resonance and therefore in absence of optical losses it is equal to $g_{rt} = r_1 r_2$.
At this point it is possible to define a further parameter to characterize an optical cavity: the finesse. The finesse is defined as:

$$\mathcal{F} \equiv \frac{\pi\sqrt{g_r t}}{1 - g_r t} = \frac{2\pi\,FSR}{\Delta\omega_{HM}} = \frac{FSR}{\Delta\nu HM} \tag{3.20}$$

The finesse provides information about the quality of the cavity's resonances. A higher finesse indicates narrower resonances and better separation between the resonant frequencies. Conversely, a lower finesse corresponds to broader resonances and less selective behavior. It is also a measure of the cavity's ability to enhance an optical signal, indeed the intensity of the field circulating in the cavity can be expressed as:

$$\frac{I_c}{I_{in}} = \frac{\mathcal{F}}{\pi} \tag{3.21}$$

when $r_1 = r_2$.

3.1.3   Stable optical resonators

As mentioned in section 2.2, the wavefront of the Gaussian beam is characterized by a certain curvature that depends on the position along the propagation direction. For this reason, for the cavity to support resonant modes, the curvature of the mirrors must match that of the beam; in this way, the possibility of radiation escaping from the resonator (walk-off) is prevented. In this section the general stability condition of a cavity formed by two spherical mirrors will be derived.
Let's consider a Gaussian beam with a wavefront having curvature radii R_1 and R_2 at positions z_1 and z_2 supported by a cavity with two spherical mirrors placed at a distance d. The condition to determine the beam waist, the beam size at the mirrors and its Rayleigh range is given by the following system of equations:

$$\begin{cases} R(z_1) = z_1 + \dfrac{z_R^2}{z_1} = -R_1 \\[2mm] R(z_2) = z_2 + \dfrac{z_R^2}{z_2} = R_2 \\[2mm] L = z_2 - z_1 \end{cases} \tag{3.22}$$

where L is the length of the cavity, $R(z_1)$ and $R(z_2)$ are the radii of curvature of the mirrors and $R(z_1)$ is required to be negative because the entering beam converges toward the center of the

cavity.

To solve this system as a function of R_1, R_2 and L it is useful to define two parameters characterizing the resonator:

$$g_1 \equiv 1 - \frac{L}{R_1}, \qquad\qquad g_2 \equiv 1 - \frac{L}{R_2} \qquad\qquad (3.23)$$

In terms of g_1 and g_2 it is easy to find that the trapped Gaussian beam must have Rayleigh range equal to:

$$z_r^2 = \frac{g_1 g_2 (1 - g_1 g_2)}{(g_1 + g_2 - 2g_1 g_2)^2} L^2 \qquad\qquad (3.24)$$

from where, remembering Equation 2.16, it is easy to obtain the beam waist as:

$$w_0^2 = \frac{L\lambda}{\pi} \sqrt{\frac{g_1 g_2 (1 - g_1 g_2)}{(g_1 + g_2 - 2g_1 g_2)^2}} \qquad\qquad (3.25)$$

Furthermore, it can be useful to know that the beam size in correspondence with the two mirrors can be computed using Equation 2.16:

$$w_1^2 = \frac{L\lambda}{\pi} \sqrt{\frac{g_2}{g_1(1 - g_1 g_2)}}, \qquad\qquad w_2^2 = \frac{L\lambda}{\pi} \sqrt{\frac{g_1}{g_2(1 - g_1 g_2)}} \qquad\qquad (3.26)$$

From the relations just obtained it is clear that a real and finite solution for the Gaussian beam exists only if $z_r^2 \geq 0$, that in terms of g_1 and g_2 corresponds to a requirement defining the stability range of the resonator:

$$0 \leq g_1 g_2 \leq 1 \qquad\qquad (3.27)$$

This condition can be graphically represented in a Cartesian plane having g_1 on the x-axis and g_2 on the y-axis (Figure 3.4):

The principal kind of resonators are:

- **Symmetric resonator**: the two mirrors have the same radius of curvature $R_1 = R_2$ and therefore also $g_1 = g_2$. In this case the waist is situated at the center of the resonator;

- **Symmetric resonator**: the entering mirror is planar $R_1 \to \infty$, thus $g_1 = 1$. The beam waist is located on the input mirror;

- **Confocal symmetric resonator**: the curvature of the mirrors is equal to the length of the cavity $R_1 = R_2 = L$ and therefore $g_1 = g_2 = 0$. This resonator is characterized by the smallest beam size and it is very robust against misalignment;

- **Near planar resonator**: in this case $R_1 = R_2 = R \gg L$ and as a consequence $g_1 = g_2 \simeq 1$. The beam supported by this cavity has a very large waist and it is very sensitive to misalignment;

- **Hemispherical resonator**: one mirror is planar $R_1 \to \infty$ while the other corresponds to $R_2 = L + \Delta L$. In this situation the beam size is small at the planar mirror and large at the curved mirror. This kind of cavity is used in gas laser to easily tune the beam size;

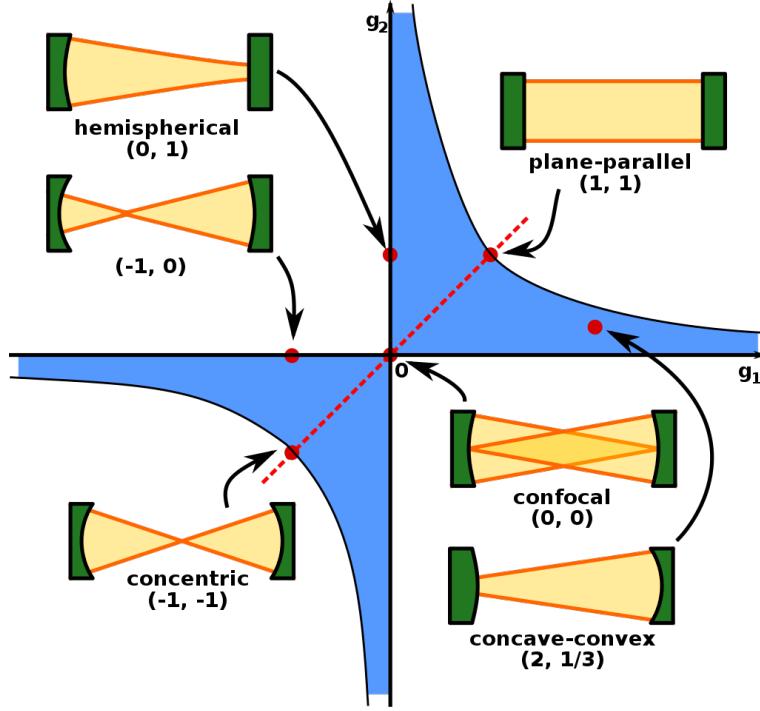- **Concave-convex resonator**: the beam waist is located outside the cavity.

Figure 3.4: Stability diagram of an optical resonator.

3.1.4   Transversal modes

The TEM00 is the fundamental eigenstate of an optical resonator. However a spherical resonator can support an infinite number of eigenstates.
The total phase shift that accumulates as the beam propagates from one mirror to the other is given by:

$$\phi(z_2 - z_1) = kL - (m + n + 1) \times [\psi(z_2) - \psi(z_1)] \tag{3.28}$$

where $\psi(z_i) = \tan^{-1}(z_i/z_R)$ is the Gouy phase.
Expressing z_1 and z_2 in terms of the g_1 and g_2 parameters of the cavity and with some algebraic steps one retrieve that the Gouy phase shift along the resonator is given by:

$$\Delta\psi = (m + n + 1)\arccos\left(\pm\sqrt{g_1 g_2}\right) \tag{3.29}$$

Therefore the resonant frequency of a mode of order m, n belonging to the axial mode of order q is written as follows:

$$\omega = \omega_{q,m,n} = \left[q + (m + n + 1)\frac{\arccos\left(\pm\sqrt{g_1 g_2}\right)}{\pi}\right]\frac{\pi c}{L} \tag{3.30}$$

The higher order modes spectrum appears as a further division into the free spectral range. There are three limiting cases, corresponding to different regions of the stability diagram, that can be analyzed and that are represented in Figure 3.5:

- **Near planar situation:** as in this case $g_1 \sim g_2 \sim 1$ then $\arccos\left(\pm\sqrt{g_1 g_2}\right) = 0$. This means that the transverse modes q,mn associated to the axial mode q are all clustered near the q,00 mode and therefore the transverse mode spacing is small compared to the axial mode spacing;

- **Confocal resonators:** in this configuration $g_1 \sim g_2 \sim 0$ then $\arccos\left(\pm\sqrt{g_1 g_2}\right) = \pi/2$. As a consequence the modes 01 and 10 associated to the q-th axial mode move out to fall between the q and the q+1 axial modes. Accordingly, the q11, q02 and q20 modes of the q-th axial mode coincide with the q+2,00 mode, and so forth;

- **Concentric resonators:** it is the situation in which $g_1 \sim g_2 \sim -1$ and thus $\arccos\left(\pm\sqrt{g_1 g_2}\right) = \pi$. It is the case opposit to the near planar situation: this time the q,mn modes will approch the q+1,mn mode from the low frequency side.
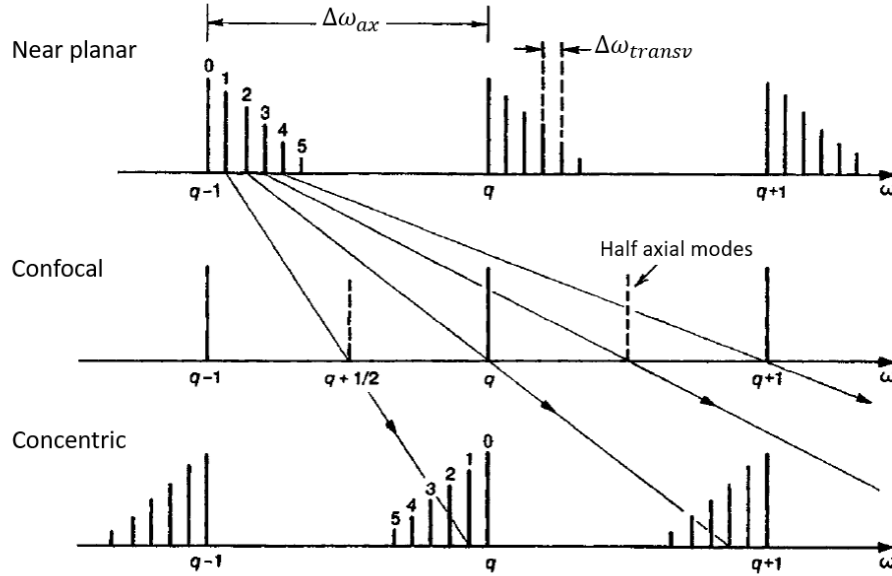
Figure 3.5: Transverse mode spacing in stable optical resonators.

3.2   Design of the test cavity

The optical cavity is the core of the experiment and it has been designed according to the equations outlined in subsection 3.1.3. The cavity is formed by two identical high reflective mirrors with radius of curvature $R = 0.2$ m and trasmissivity $T = 1 - |r|^2 = 0.0002$. The choice of these mirrors is dictated by the fact that the finesse of the cavity has to be quite high to allow to measure its variation when the membrane is inserted in the cavity. Indeed, as the coating membrane is characterized by a certain absorption, we expect the finesse to diminish when the membrane is placed between the two mirrors.
The theoretical finesse of the empty cavity, assuming zero losses, is equal to:

$$\mathcal{F} = \pi \frac{r}{1 - r^2} = 15706 \tag{3.31}$$

The length of the cavity was chosen taking into consideration both the dimension of the cryostat experimental plate and the lens availability in the laboratory.
Indeed, the cavity has to be mounted inside a cryostat that has a diameter of 250 mm. Considering the situation in which the center of the cavity coincides with the center of the cryostat breadboard, the length of the cavity can be chosen in the range between 21 cm and 6 cm. The minimum length value is chosen considering the fact that enough space has to be left between the mirrors in order to install the membrane and its piezo-actuators.
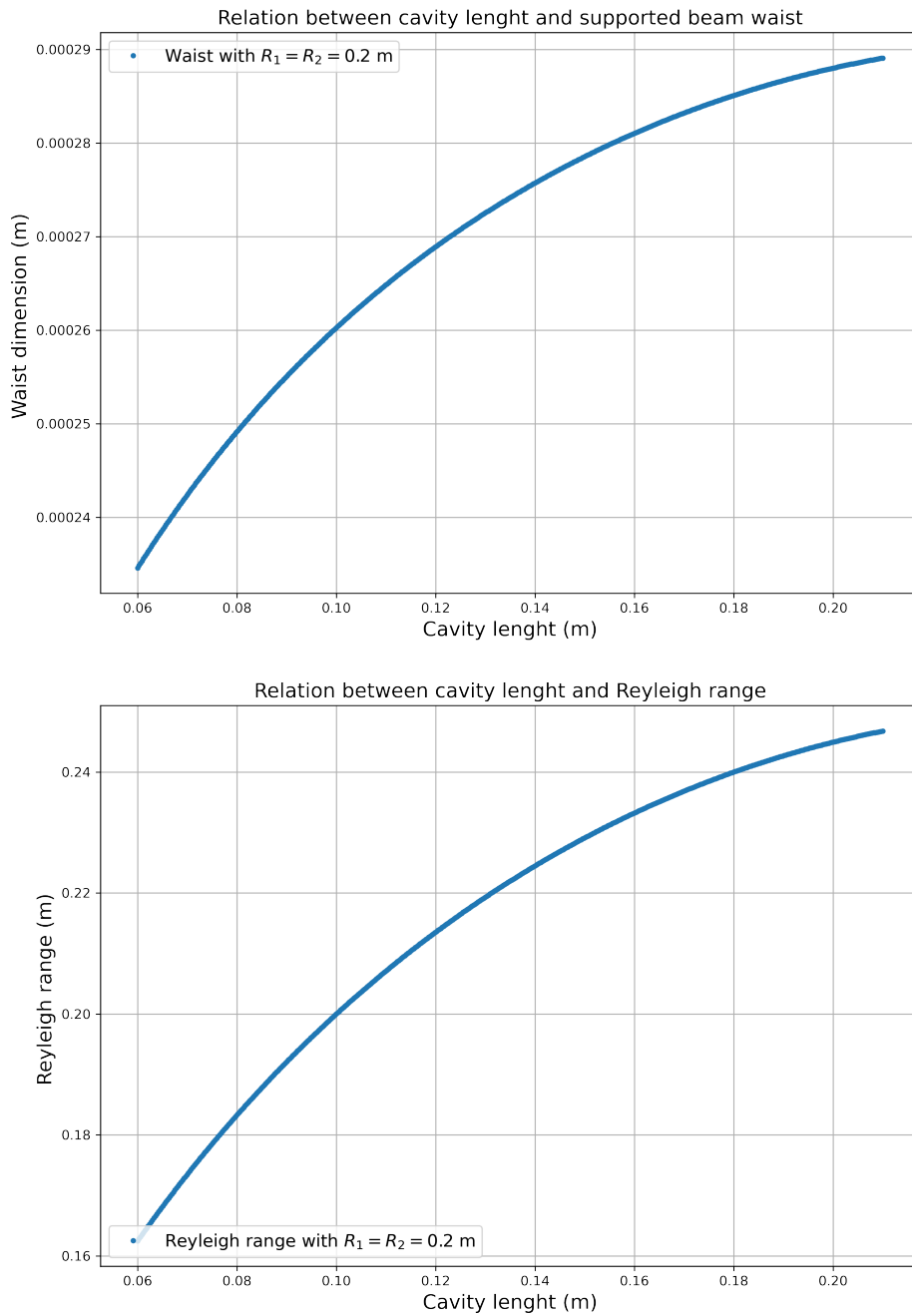
Figure 3.6: The plot shows how the waist and the Rayleigh range of the beam supported by the cavity vary according to length of the cavity.

Considering this length constrain and the radius of curvature of the mirrors it is possible to calculate for each length the values g_1 and g_2 defining the resonators (see Equation 3.23) and verify the stability of the cavity with the relation:

$$0 \leq g_1 g_2 \leq 1 \tag{3.32}$$

The parameters g_1 and g_2 can also be used to study how the waist and the Rayleigh range of the beam supported by the cavity depend on the length of the resonator. This calculation is performed using Equation 3.24 and Equation 3.25; the results are plotted in Figure 3.6 and they will be also used to decide which is the correct lens arrangement allowing to have an initial beam that matches the cavity.

A further parameter that must be controlled in order to chose the length of the cavity is the higher order modes spacing, i.e. the frequency difference between adjacent higher-order modes of the cavity. Having enough distance between the modes allows to obtain more easily a single longitudinal mode in transmission from the cavity. The equation to calculate the higher order modes spacing is the following:

$$\Delta\omega_{HOM} = \frac{FSR}{\pi} \arccos \sqrt{g_1 g_2} \tag{3.33}$$

The final length chosen for the cavity is $L = 10.6$ cm, which corresponds to a supported beam with a waist equal to $w_0 = 263\,\mu m$.

The free spectral range of this cavity corresponds to:

$$FSR = \frac{c}{2L} = 1.42\,GHz \tag{3.34}$$

while the higher order modes spacing is equal to $\Delta\omega_{HOM} = 487\,MHz$. As the finesse can be calculated also as the ratio between the FSR and the width of the resonance peak, it is possible to verify that this value of $\Delta\omega_{HOM}$ prevents to have mode overlapping:

$$\delta\omega = \frac{FSR}{\mathcal{F}} = 0.09\,MHz \tag{3.35}$$

where $\delta\omega$ is the expected full width at half maximum of the resonance peak.

3.3   Effect of a membrane on the cavity finesse

In this section the effect of the imaginary part of the membrane's refraction index on the finesse of the cavity will be explained.

3.3.1   Optical characteristics of a membrane

A flat membrane, from the optical point of view, behaves as an ethalon, which is an optical interferometer. The Fresnel coefficients describe the behavior of light as it passes through the interface between two media with different refractive indices. When dealing with thin films, such as a flat membrane, the Fresnel equations need to be extended to account for multiple reflections within the film. The equations needs also to consider the phase change that occurs upon reflection from the front and back surfaces of the thin film. For a thin film of thickness d and refractive index n, placed between two media (in this case air with refractive index ~ 1), the reflection and transmission coefficient of the film can be calculated using the following equations [12]:

$$r = \frac{r_1 + r_2 e^{2i\delta}}{1 + r_1 r_2 e^{2i\delta}} \tag{3.36}$$

$$t = \frac{t_1 t_2 e^{i\delta}}{1 + r_1 r_2 e^{2i\delta}} \tag{3.37}$$

where r_1 is the reflection coefficient at the front surface (air to film interface), r_2 is the reflection coefficient at the back surface (film to air interface), t_1 is the transmission coefficient at the front surface and t_2 is the transmission coefficient at the back surface; δ is the phase shift due to the optical path difference in the film: $\delta = knd$, with k the wave vector of the incident light.

Assuming now to describe a material characterized with a certain level of absorption or loss of energy as light passes through it, the reflection coefficients at the different surfaces can be written as a function of the complex refractive indices $n_1 = n_{R1} + i n_{I1}$ and $n_2 = n_{R2} + i n_{I2}$ as:

$$r_1 = \frac{n_1 \cos\theta_1 - n_2 \cos\theta_2}{n_1 \cos\theta_1 + n_2 \cos\theta_2} \tag{3.38}$$

$$r_2 = \frac{n_2 \cos\theta_1 - n_1 \cos\theta_2}{n_2 \cos\theta_1 + n_1 \cos\theta_2} \tag{3.39}$$

where θ_1 and θ_2 are the angles of incidence and transmission respectively.

Considering the situation of normal incidence on the membrane with index of refraction $n = n_R + i n_I$ it is possible to calculate the reflectivity and the trasmissivity of the membrane as:

$$r_m = \frac{(n^2 - 1)\sin knd}{2in \cos knd + (n^2 + 1)\sin knd} \tag{3.40}$$

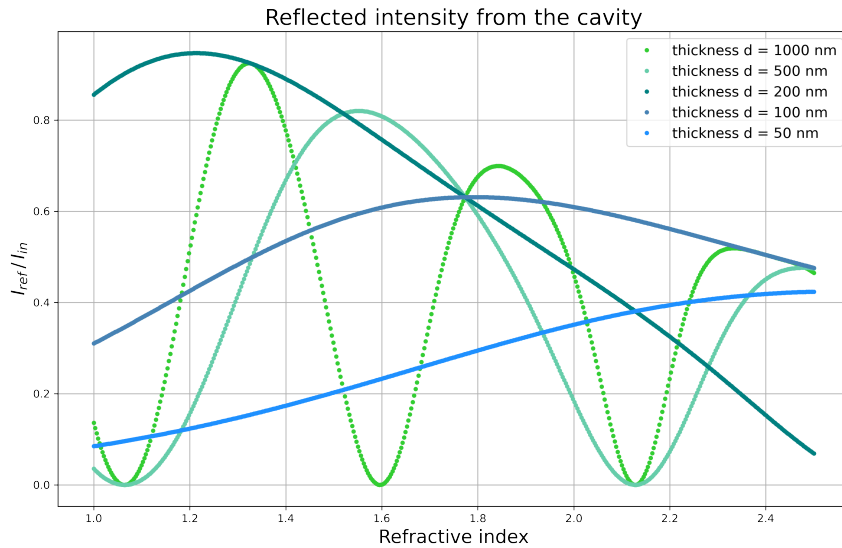$$t_m = \frac{2n}{2in \cos knd + (n^2 + 1)\sin knd} \tag{3.41}$$

Figure 3.7: $|r_m|^2$ as a function of n_R for different values of the thickness d

Assuming that $n_I = 0$ it can be seen that the reflectivity of the membrane for a fixed value of n_R, can be chosen by suitably selecting the thickness (shown in Figure 3.7).

3.3.2   Numerical study of the cavity with the membrane in the middle

The system formed by the optical cavity with the membrane inside can be considered as a two coupled cavities system, visible in Figure 3.8.
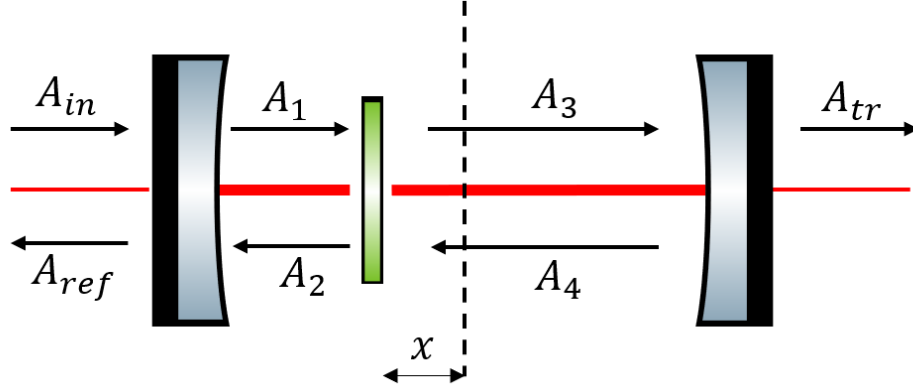

Figure 3.8: Scheme of the electromagnetic fields circulating inside the system formed by cavity and membrane.

The system of equations that describes how the transmissivity and reflectivity of the cavity change according to the membrane position is the following:

$$
\begin{cases}
A_1 = it A_{in} + r A_2 e^{ikL_1} \\
A_2 = r_m A_1 e^{ikL_1} + it_m A_4 e^{ikL_2} \\
A_3 = it_m A_1 e^{ikL_1} + r_m A_4 e^{ikL_2} \\
A_4 = r A_3 e^{ikL_2} \\
A_{ref} = it A_2 e^{ikL_1} + r A_{in} \\
A_{tr} = it A_3 e^{ikL_2}
\end{cases}
\tag{3.42}
$$

where r_m and t_m are the reflection and transmission coefficients of the membrane, A_{in}, A_{ref} and A_{tr} are the incident, reflected and transmitted fields while A_1, A_2, A_3 and A_4 are the circulating fields; r and t are the reflection and transmission coefficients of the cavity's mirrors. The initial position of the membrane is at the center of the cavity, therefore at $x = 0$; every time the membrane is shifted of a quantity x, the lengths L_1 and L_2 of the two coupled cavities changes, always keeping $L = L_1 + L_2$ fixed.

The solution of this linear system can be found with the Cramer's method using as variables the wavevector k and the incident power.

To predict the behaviour of the system built in the laboratory these equations are solved using the following values:

- Cavity length: $L = 10.6$ cm

- Mirrors radius of curvature: $R_{curv} = 0.2$ m

- Mirrors reflectivity: $R_1 = R_2 = 99.98\%$

With this initial parameters the values expected for the Free Spectral Range and the finesse $\mathcal{F}$ of the system are: $FSR = 1.42\,GHz$ and $\mathcal{F} = 15706$.

To reproduce the displacement of the membrane inside the optical cavity, the linear system in

Equation 3.42 has to be solved for every membrane position, which correspond to vary the value of the length L_1 (and accordingly also the value of L_2).

For each of the membrane positions, the transmitted power $|A_{tr}|^2$ is obtained as a function of the incident power and of the wavevector k. In this way it is possible to find the numerical values k_0 for which the output power is maximum (the optical resonances) and also the value δk for which:

$$|A_{tr}(k_0 + \delta k/2)|^2 = \frac{|A_{tr}(k_0)|^2}{2} \tag{3.43}$$

therefore δ_k corresponds to the width of the resonance peak at half of its maximum value.
The finesse is calculated as:

$$\mathcal{F} = \frac{2\pi}{c} \frac{FSR}{\delta k} \tag{3.44}$$

where FSR is the free spectral range, i.e. the distance between two resonance peaks. As the reflectivity of the membrane is very small, it can be assumed that the FSR of the cavity does not change when the membrane is inserted between the mirrors.

The finesse evolution as a function of the membrane displacement obtained with this model is shown in Figure 3.9. As expected, due to the fact that the radiation wavelength is $\lambda = 1064$ nm, the modulation is characterized by a period of 500 nm.
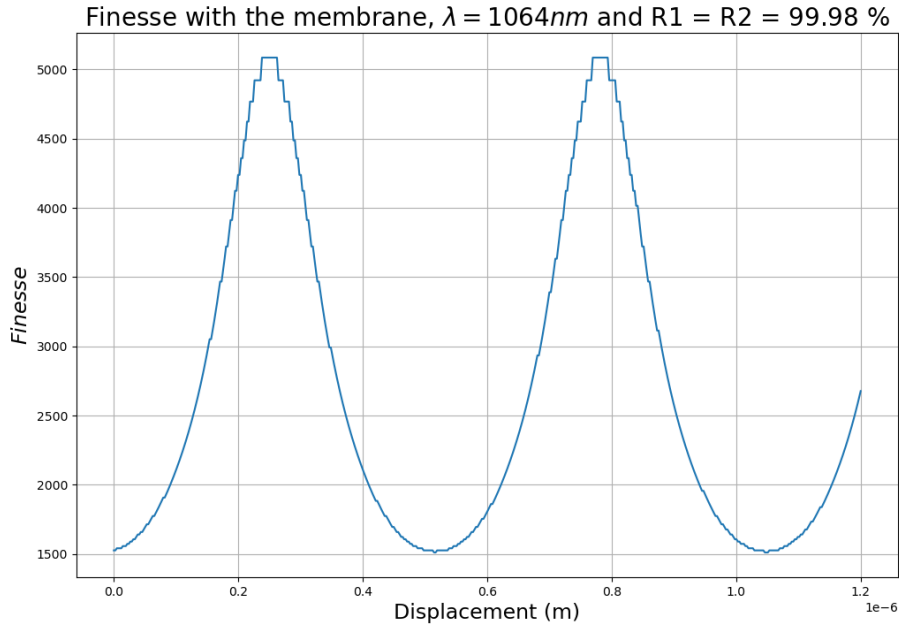

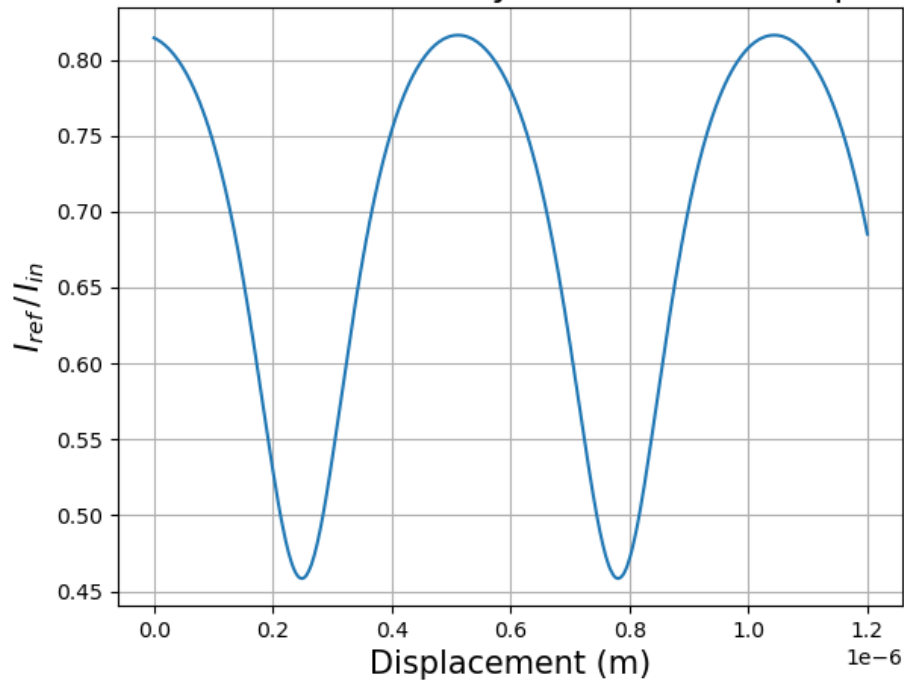Figure 3.9: Simulated finesse as a function of the displacement of the membrane.

As explained above, also the transmitted and reflected power depend on the membrane position and the modulation period is equal to that of the finesse, as visible in .

The finesse of the cavity with the membrane can also be calculated analytically using Gaussian optics. In this case the finesse and the optical resonant frequencies are calculated as a function of the membrane position z_0 imposing boundary conditions to the cavity fields.

$$\frac{1}{\mathcal{F}_m(z_0)} = \frac{1}{\mathcal{F}_{empty}} + \frac{2}{\pi} \left| \Im \left[\frac{L\delta\omega(z_0)}{c} \right] \right| \tag{3.45}$$

40

were the function $\delta\omega(z_0)$ depends on the refractive index and on the thickness of the membrane and on the radiation wavelength. Using Equation 3.45 to fit the experimental data it will be possible to retrieve the imaginary part of the membrane's refractive index.
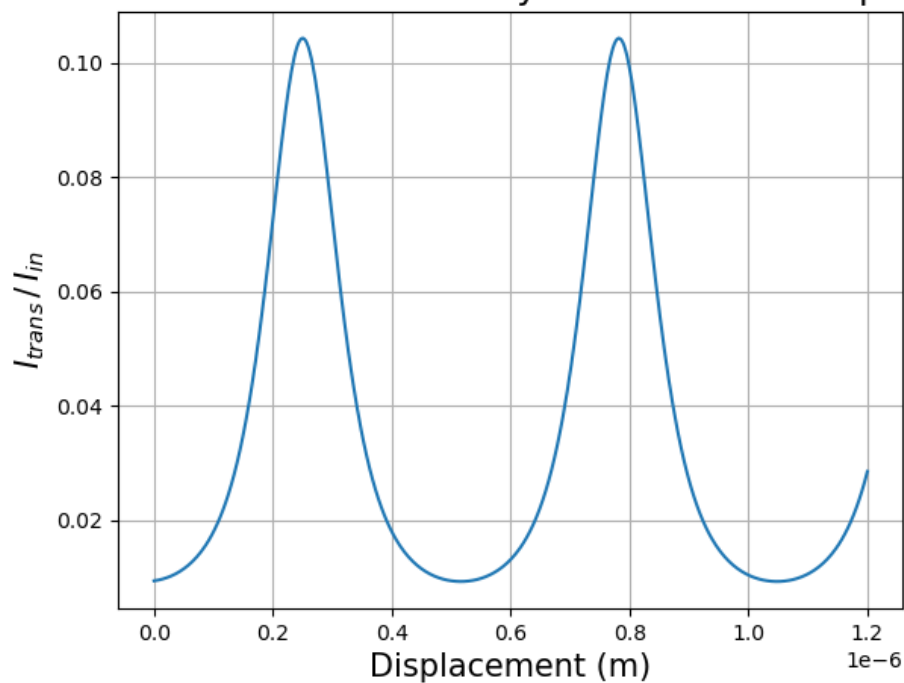

Figure 3.10: Simulated on resonance reflected and transmitted power as a function of the displacement of the membrane.

Chapter 4

Experimental set-up

4.1 Introduction to the measurement method

As already mentioned in the first chapter, the need to perform a direct measurement of the mechanical and optical losses of a coating without including the substrate effect, has stimulated the development of a new experimental setups to characterize different coatings.

This innovative experimental setup allows to measure simultaneously the optical losses and the mechanical losses of a free standing coating membrane, both at room and at cryogenic temperature, by greatly limiting the influence of the substrate on the results. To achieve this result the apparatus includes a low-vibration cryostat, where the sample can reach a nominal temperature of 4 K, inside of which an optical cavity is installed.

The membrane to be tested is positioned within the optical cavity and it can be displaced along the optical axis of the cavity by means of precise nano-positioning systems, so that it can interact with the intra-cavity field. Indeed, as the membrane is characterized by specific reflection, transmission and absorption coefficients, when the membrane is placed in the cavity it has the effect of modifying the value of the transmitted and reflected intensity from the cavity. Consequently, also the finesse value gets modified. By considering this system as two coupled cavities, it is possible to estimate the finesse variation as a function of the membrane position.

In particular, when a membrane is placed inside the cavity the transmitted intensity, and also the finesse, are reduced due to the absorption of the membrane; however, this effect is minimized when the membrane position coincides with a minimum of the stationary electromagnetic field resonating inside the cavity. This is in fact the situation in which the coupling between the cavity and the membrane is at its lowest. Thus, we expect to observe an oscillating behaviour of the finesse according to the displacement of the membrane with respect to the maxima and minima pattern of the electromagnetic field.

The second part of the experiment, that is however not included in this thesis, will focus on measuring the mechanical dissipations. Indeed, the resonant frequencies and the mechanical loss angle of the membrane can be obtained measuring the output power of the cavity at resonance. As for the finesse, also the transmitted power depends on the displacement of the membrane inside the cavity. This relation allows to transduce the vibrational signal of the membrane in an optical signal measurable with a photodiode. Again, this can be done exciting the resonances of the membrane through the piezo actuator.

The membrane characteristics and the description of the experimental apparatus will be provided in the next paragraphs.

4.1.1 The membranes

The goal of this experiment is the study of the optical losses of silicon nitride (SiN) membranes. Samples from two producers has been used: the ones fabricated by the private company (Norcada) and those manufactured by the Fondazione Bruno Kessler in Trento. The first measurement will be performed on a Norcada's membrane; this choice was made considering the fact that these membranes have already been tested by other groups and therefore, by cross-checking the results, it is possible to get some feedback on the accuracy of the experimental apparatus.

The samples consist in a window (2×2 mm or 5×5 mm) covered by a freestanding membrane of silicon nitride. In particular the ones from Norcada are high-stress, non stoichiometric membranes (also soichiometric membrane are available) of different thickness (1 μm, 500 nm, 200 nm, 100 nm and 50 nm).

The positioning of the membrane inside the cavity is performed through some piezoelectric actuators: the Attocube x-Scanner allows to control the movement of the membrane along the optical axis of the cavity, while the SmarAct Tip-Tilt-Mirror mount allows to adjust the inclination angle with respect to the cavity axis. This last mount will be very important to maintain the membrane perpendicular to the beam propagation direction, in order to reduce as much as possible the losses due to any misalignement that may occur during the experiment.

As the tip-tilt-mirror is not yet available, for the moment the membrane has been glued on a mirror mount that allows to adjust the inclination angle vie three screws. A picture of the membrane is visible in Figure 4.1.

The estimation of the optical absorption is facilitated when $r_m \sim 0$, and for this reason the first measurement will be performed using a Norcada membrane of thickness 500 nm, for which we expect a reflectivity $r_m \simeq 0.0004$ when assuming $n_R \sim 2$.

Analyzing Equation 3.40 more in depth, it can be seen that the reflectivity when $n_I \neq 0$ differs from the one with $n_I = 0$ of a quantity proportional to n_I/n_R. However, the expected value of n_I is around 10^{-5}, thus it is possible to approximate the reflectivity of the membranes with the function calculated for $n_I = 0$.
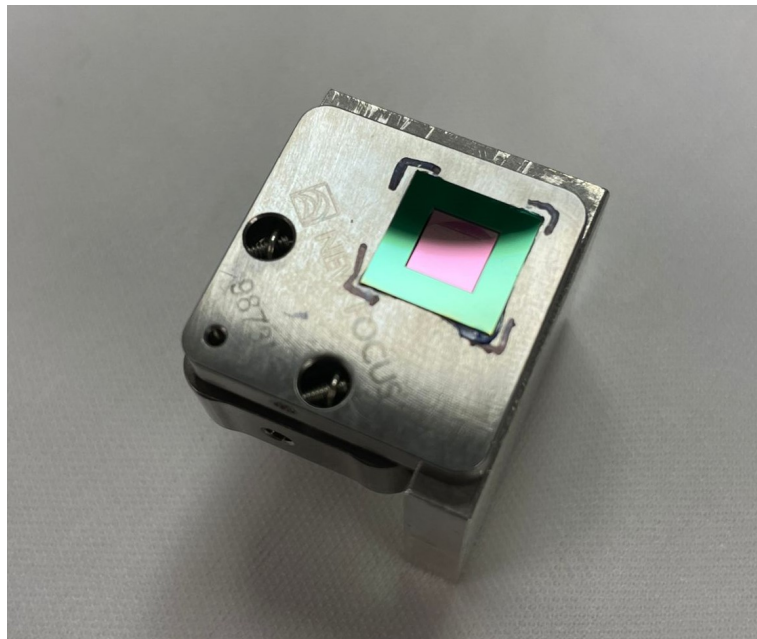

Figure 4.1: Norcada membrane of thickness equal to 500 nm glued on a mirror mount.

4.2   Description of the optical bench

4.2.1   Scheme of the optical line

The optical line constructed for this experiment is divided between two optical benches. Indeed, the laser is shared with a different experiment and for this reason it was necessary to use an optical fiber to create a laser pick-off arriving at the table where the cryostat is placed. The optical line built after the fiber output is shown in Figure 4.2.
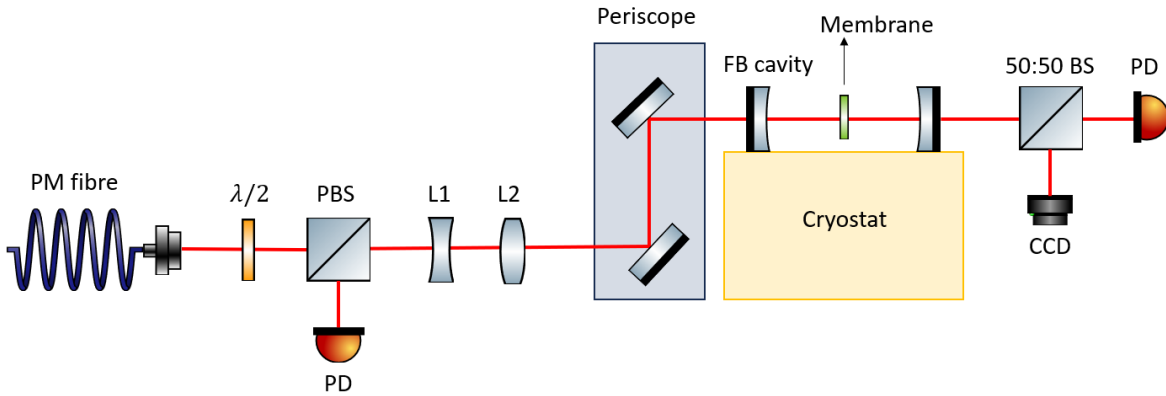

Figure 4.2: Scheme of the optical line after the fiber output.

The elements used in the optical line are the following:

- **The infrared laser:**

  The laser we use is a "Coherent" product, model Mephisto 500NE, with a nominal power of 0.525 W at a wavelenght $\lambda = 1064$ nm. This laser consists of a monolithic Nd:YAG crystal, in which atoms of Neodymium, added to a crystal of yttrium aluminate, are responsible of the light emission at the wavelength of 1064nm. It is based on a non-planar ring oscillator (NPRO) and it is further improved by a Noise Eater (NE) technology. The design of the laser cavity helps to eliminate mode competition and results in single-frequency operation. In fact, the non-planar ring geometry, along with the use of specific techniques such as Faraday isolators, ensures that only one longitudinal mode is oscillating in the laser cavity. This leads to a significantly narrower linewidth compared to traditional laser designs (≤ 3 kHz).
  Furthermore, the short round-trip length translates in a relatively large free spectral range, which allows for continuous frequency tuning over several gigahertz. The frequency tuning can be achieved in two ways: a slow method and a fast method. The slow method consists in changing the temperature of the monolithic laser crystal by applying a voltage to a peltier element in the range $-10V$ to $10V$. In particular the temperature can be changed of 0.1889 K/V while the frequency changes of -3 GHz/K at 1064 nm. Figure 4.3 shows how the frequency varies according to the temperature: the unfilled dots represents the so called modes hopes, where the laser frequency changes from one longitudinal mode to the next.
  The control of the emission's frequency of the laser can be done more quickly through a piezoelectric actuator placed on the laser crystal. Applying a voltage to the piezo crystal it is possible to contract or expand the crystal: in this way the frequency of the laser can be varied of about 2.5 MHz/V.
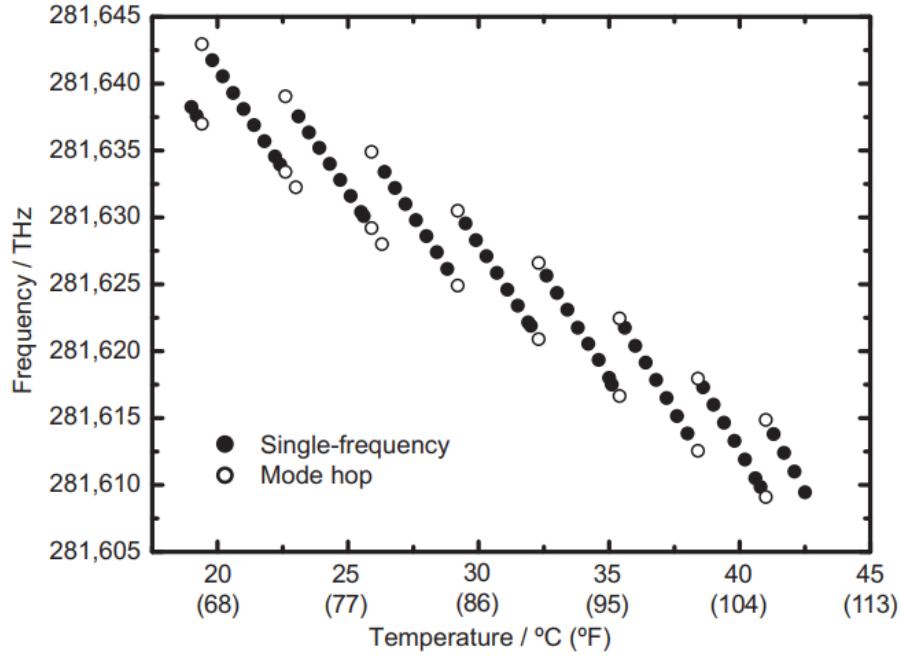
Figure 4.3: Temperature tuning of the laser crystal

- **The Polarization maintaining fiber cable:**
  The employed optical fiber is a Thorlabs product, model P3-1064PM-FC-10. It is a polarization maintaining fiber with FC/APC connectors on both ends. According to the fiber specifications the mode field diameter (MFD) at 1064 nm is equal to $10.1 \pm 0.4\,\mu m$, the numerical aperture is of 0.125 and the cutoff wavelength is 1380 nm. The numerical aperture NA of a single mode fiber describes the angle of beam divergence of the Gaussian shaped beam that is emitted by the fiber and is dfined as the sine of half the angle of beam divergence: $NA = \sin \alpha/2$.

  To couple more efficiently the laser to the fiber we decided to use the collimator PAF2-A7C, which contains an aspheric lens of focal lenght 7.5 mm. The collimator position can be adjusted relative to the fiber by a micro-positioning system with 5 degrees of freedom. The 5 axis can be regulated using five different screws: one moves the inside lens in the x direction, one in the y direction and the remaining three can be used to tilt the plate with respect to the beam propagation axis.

  The beam injected into the collimator is defined by the following parameters:

$$w_{0x} = 0.438mm, \qquad z_{0x} = 79.2cm, \qquad z_{Rx} = 56.65cm$$
$$w_{0y} = 0.405mm, \qquad z_{0y} = 78.4cm, \qquad z_{Ry} = 48.4cm$$

  where w_{0x} and w_{0y} are the values of the beam waist along the x and y directions and z_{0x} and z_{0y} are the values of the waist positions, with respect to the collimator position, in the x and y directions.

  To match the input beam conditions of the collimator that requires a beam divergence $\theta \sim$ 1.387 mrad we used a telescope made of two lenses: the first lens with focal length $f_1 = 300$ placed at a distance $z_1 = 92$ cm from the collimator and the second lens with $f_2 = 200$ placed at a distance $z_2 = 39$ cm from the collimator. In this way the final beam has a waist of $250\,\mu m$

in adn a divergence ~ 1.3 mrad) in the position where the collimator and the fiber are placed. With this configuration we reached a coupling of $\sim 15\%$. The correct positions of the lenses where calculated using the program Just Another Mode Matching Tool and the design of the telescope is presented in Figure 4.4.
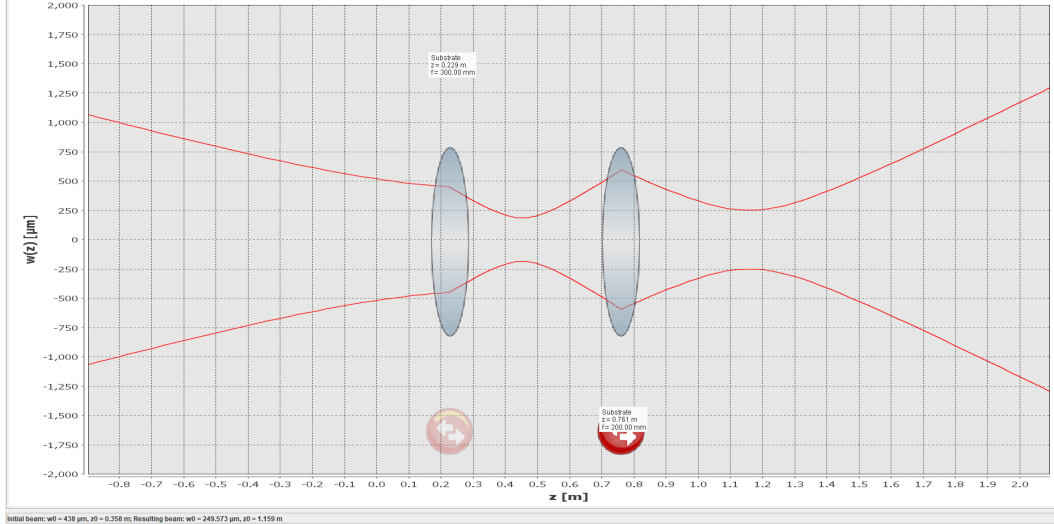

Figure 4.4: Telescope design made using the JAMMT software.

- **The half-wave plate and the polarizing beam splitter**:
  The half wave plate (indicated as $\lambda/2$ in Figure 4.2) is a retarder plate that introduces a phase shift equal to π between the two polarization components that are parallel and perpendicular to its fast axis, respectively. It can be used to rotate the polarization angle of a linearly polarized beam.
  The polarizing beam splitter (PBS) splits an incoming light beam into two beams with orthogonal polarization states.
  These two devices together constitute a useful tool that allows to adjust the power of the light injected in the cavity.

- **Lenses L1 and L2**:
  This telescope is studied to match the waist of the beam obtained in output from the fiber with the one supported by the cavity.
  To know the parameters defining the beam coming from the fiber output it is necessary to perform a beam scan. This is done by measuring the beam waist at different positions from the source by means of an instrument called beam profiler. The function used for the fit is then the following:

$$w(z) = \omega_0 \sqrt{1 + \left[\frac{\lambda(z - z_0)}{\pi \omega_0^2}\right]^2} \tag{4.1}$$

where ω_0 and z_0 are the parameters to obtain. In this case the values obtained for the waist is $\omega_0 = 324 \pm 5\,\mu m$ and it is placed at $z_0 = 9.6 \pm 0.8$ cm from the fiber output collimator; the Rayleigh range is equal to $z_R = 31 \pm 1 cm$ The fit performed with the pairs of value measured in the far field region of the beam is shown in Figure 4.5.
At this point using a second mode matching software it is possible to calculate the positions and the focal length of the lenses necessary to match this beam inside the cavity. Knowing

that the cavity center is placed at a distance of 94 cm from the fiber output and that the waist of the TEM00 cavity mode is $w_{cavity} = 269\mu m$, the telescope that can transform correctly the beam is formed by a firts lens with negative focal length $f_1 = -50$ mm, placed at $z_1 = 11.6$ cm from the fiber and a second length with positive focal lenght $f_2 = 100$ mm placed at a distance $z_2 = 69.1$ cm from the fiber.

With this telescope the waist of the resulting beam is equal to $w_{final} = 270\mu m$ and it is situated at $z = 92.6$ cm from the fiber output. The effect of the telescope is visible in Figure 4.6.
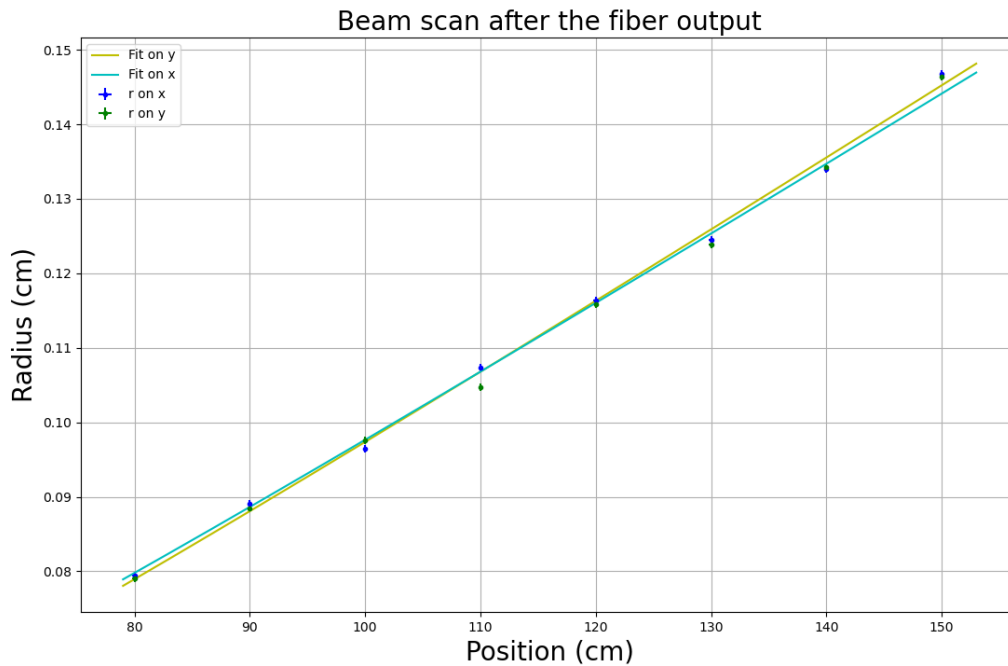
Figure 4.5: Beam scan performed in the far field region of the beam emitted from the fiber output.
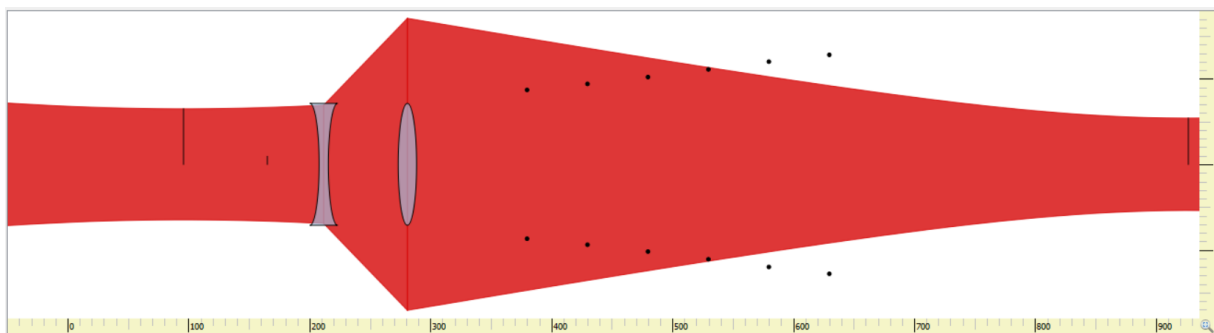
Figure 4.6: Effect of the telescope on the initial beam as calculated by the Gaussian Beam software.

- **The periscope:** As the height of the cryostate windows do not coincides with the height of the optical elements placed on the optical bench it has been necessary to design and build

a periscope to bring the light beam to the correct position. The periscope is a very stable Thorlabs product specifically chosen to reduce the effect of the environmental vibrations.The two 45° reflective mirrors are screwed on the vertical plate constituting the periscope. A picture of the structure is visible in Figure 4.7.
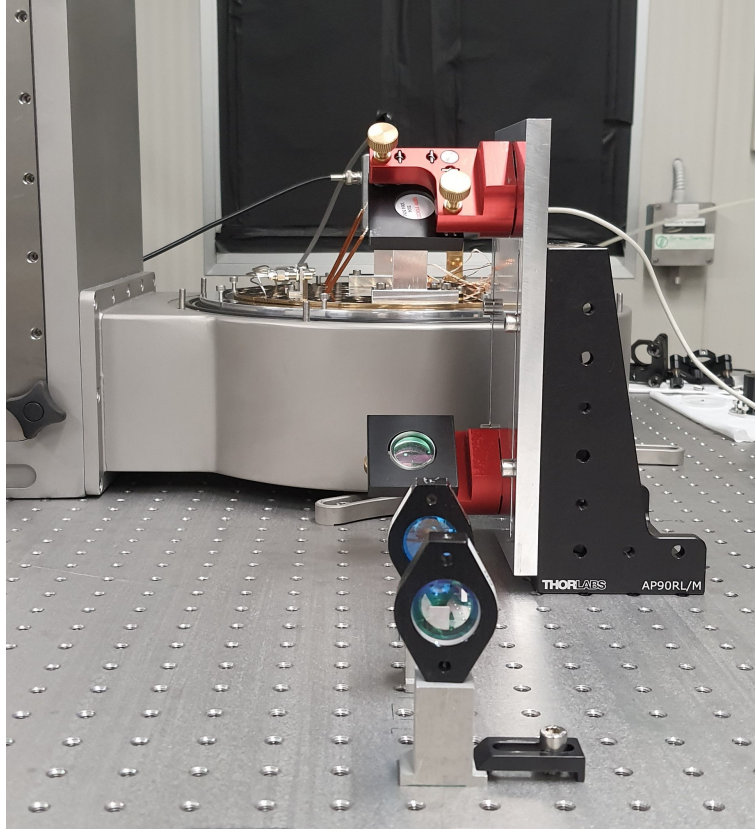

Figure 4.7: Picture of the telescope as seen from the fiber side.

- **Fabry-Perot cavity:**
  The final cavity is a monolithic cavity with a length of 10.6 cm, a waist of $w_{cavity} = 263 \mu m$ as already specified in section 3.2.

- **The photodiode:**
  This is a photodetector used to measure the output signal from the cavity. There is no need to place any lens before the photodiode as its active area is quite big compared with the beam dimension.
  A second photodiode is placed on the free side of the PBS to detect the beam reflected from the cavity; it will be used in the next phase of the experiment to locked the laser to the cavity length.

4.2.2 Cryostat characterization

The cryostat in use in the laboratory is a product of the Optidry series of the MyCryoFirm company based on a Pulse Tube Cryocooler (PTC). It is composed of two parts that can be independently configured. The first one is the Cryocase, a rectangular case in stainless steel with removable panels allowing easy access to cold areas. One of the faces of the Cryocase is connected to the low vibrations experimental chamber, the Cryobreadboard. The latter is formed by a plate of 250 mm with the tapped holes characteristic of an optical bench; its cover is equipped with eight

optical accesses placed at a height of 188 mm and a vertical access. Three internal connectors of 24 pins are provided for temperature control (thermometers and heaters), DC wires (constantan loom) and/or piezo connections (copper loom).

The PTC is composed of a water cooled compressor connected to a cold head supplying two cold stages. The temperature of the first stage is around 50K and is used as a cold shield and as a thermalization stage for cables or other components that do not need an optical access. The second stage has a base temperature below 4.2K and is connected to the cold experimental breadboard. A schematic image of the cryostat is visible in Figure 4.8.

The cryostat is connected to a vacuum system composed of a dry primary pump and a compact turbomolecular pump.
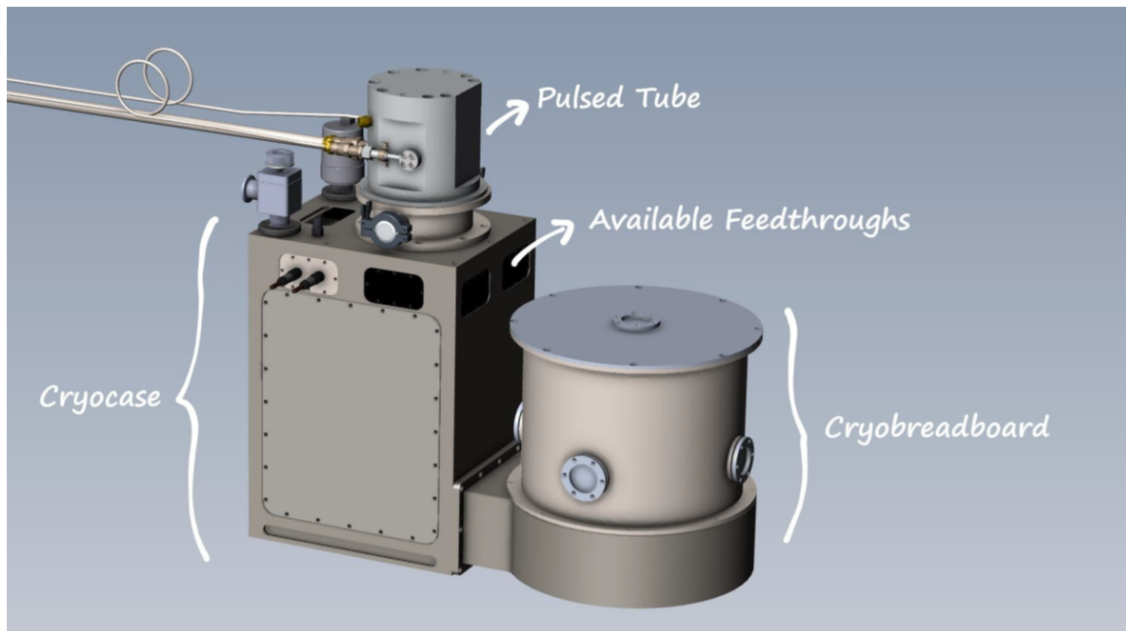

Figure 4.8: Global view of the cryostat

The cryostat was used for the first time during this experiment and for this reason the initial part of the thesis activities was dedicated to characterize the vacuum system and the proper working of the cooling and heating system.

Before switching on the compressor that cools the system, the vacuum level inside the chamber must reach a value lower then 10^{-3} mbar. At this point the cryogenic system employs about eight hours to reach its minimum temperature and the pressure stabilizes at 4×10^{-8} mbar. Three different thermometers monitor the temperature inside the cryostat: one is positioned on the chamber shield whose minimum temperature is 30 K, one is placed on the breadboard plate (where the temperature can reach 3 K) and the last can be attached close to the analyzed sample. The rate of reduction of the temperature measured by these three thermometers is plotted in Figure 4.9.

Another interesting characteristic of the cryostat is the possibility to modify the temperature of the sample acting on some heaters, whose working point is stabilized by a PID control system. This feature allows to change the sample temperature while keeping fixed the temperature of the shield and the plate. The proper working of these control loops were tested bringing the temperature of a trial sample to different final values and varying the parameters of the PID control system. An example is visible in Figure 4.10, where the sample reaches the temperature of 20 K after few oscillations around the set value.
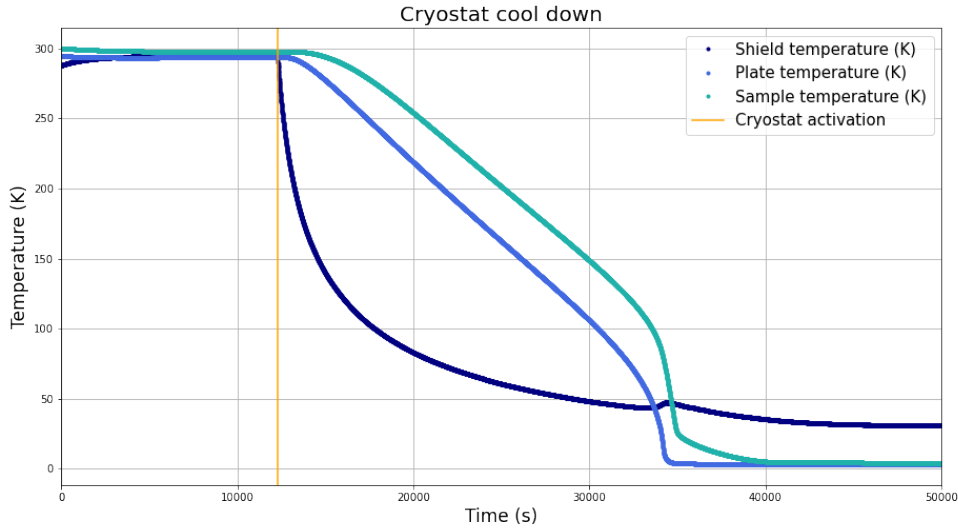
Figure 4.9: Temperature evolution inside the cryostat when the compressor is switched on: the three different curves represent the temperature of different zones of the experimental chamber.
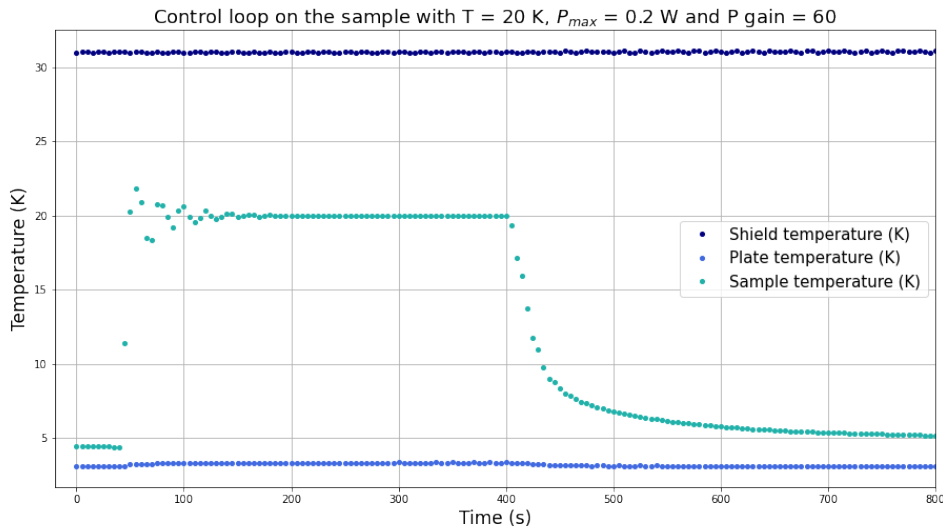

Figure 4.10: The plot shows how the temperature of the sample increases from 4 K to 20 K when the heater is activated. Before stabilizing at the requested temperature the system is subjected to a certain number of oscillation that depends on the value assigned to the P gain of the PID controller. After 400 seconds the heater is turned off and the temperature diminishes again. In this case the sample the heater acts on a trial sample which is a rectangular metal plate with sides of few centimeters.

4.2.3 Optical cavity characterization

According to the initial project, the two mirrors composing the cavity had to be mounted on two separated pillars, placed at a distance of 16 cm (see Figure 4.11). With this length choice the waist at the center of the cavity had to be equal to $w_0 = 281\,\mu m$. In this case the membrane had to

be placed in the middle of the cavity on an independent support appropriately designed to fit also the piezo actuators.
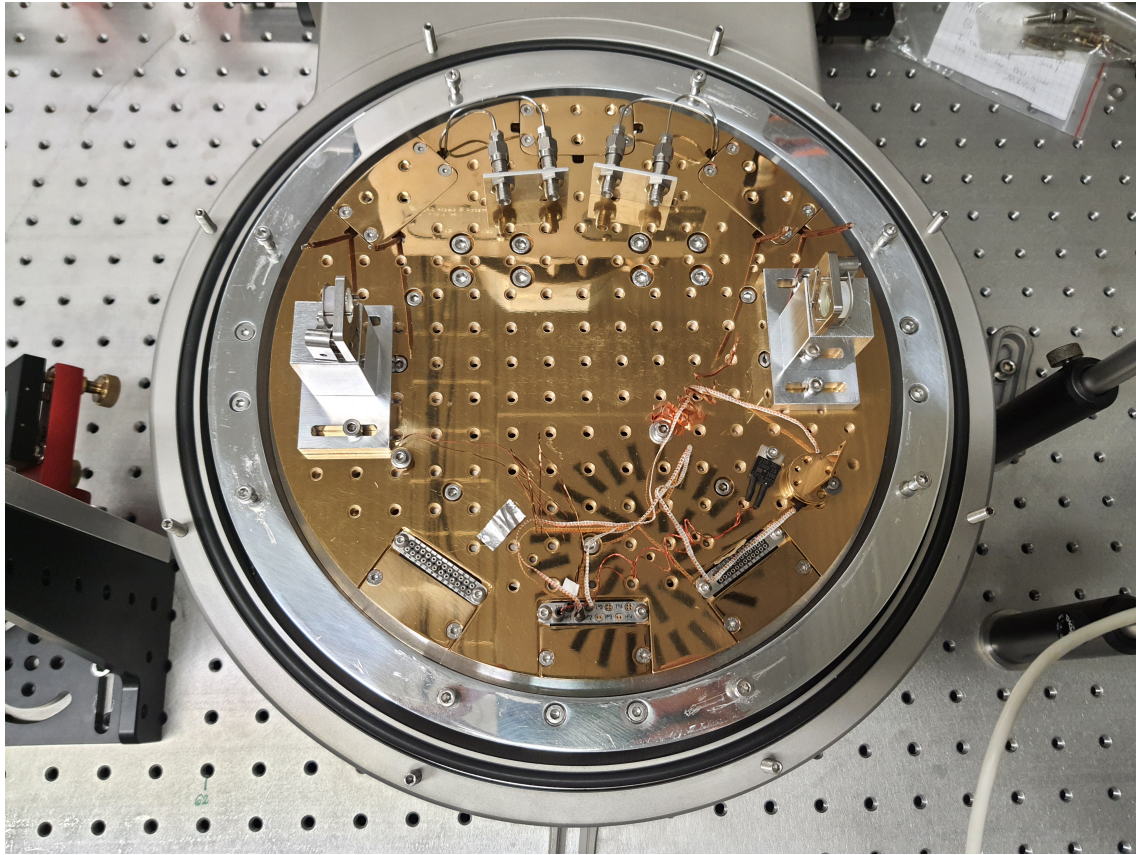

Figure 4.11: Picture of the original open cavity placed inside the cryostat.

Unfortunately this design has proved to be very noisy due to the independent vibrations of one mirror with respect to the other. This problem has been noticed when the finesse of the cavity was measured for the first time.

As already explained in section 3.2, the finesse is calculated as the ratio between the free spectral range and the width of the resonance peak and these two values can be obtain by 'scanning the cavity'. The frequency scan of the cavity is performed in two different ways depending on whether the parameter to be measured is the FSR or the resonant peak width:

- To measure the FSR a triangular voltage signal is sent to the temperature control of the laser crystal. In this way the laser frequency varies of about $0.57\,GHz/V$ and with a triangular signal of about $3\,V$ peak to peak it is possible to visualize one free spectral range;

- To measure the full width at half maximum of the resonance peak a triangular voltage is sent to the piezo actuator of the laser crystal, after having manually tuned the laser frequency close to one of the cavity resonances. With this method it is possible to span a smaller frequency range, about 10 MHz with a triangular signal with peak to peak amplitude of 4 V.

Of course, in both cases, the signal transmitted from the cavity and detected by the photodiode is analyzed with an oscilloscope.

The signal obtained when measuring the free spectral range of this first cavity is plotted in Figure 4.12.
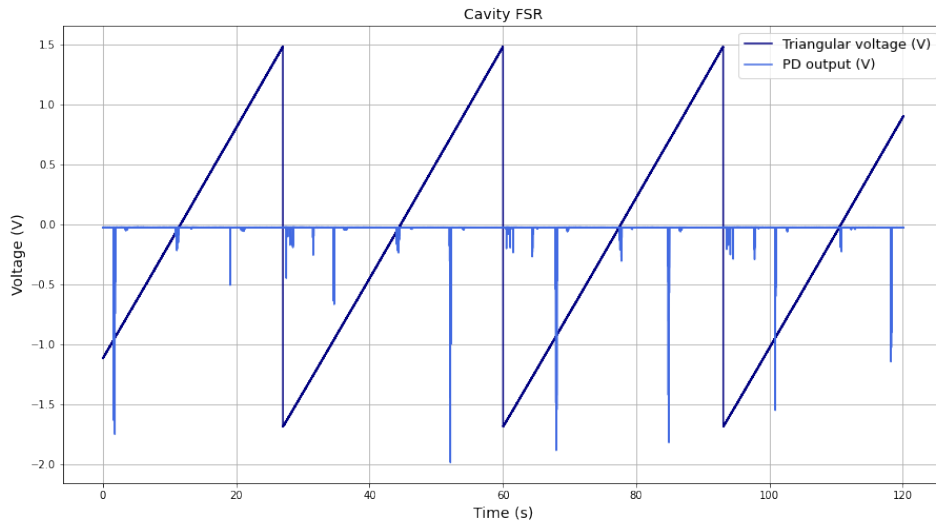
Figure 4.12: Transmitted signal when scanning the cavity by changing the laser's crystal temperature.

When a laser beam is perfectly matched to a cavity only the fundamental TEM00 mode resonates in it. As in this case the beam is not perfectly matched and aligned to the cavity, in addition to the peak corresponding to the TEM00 mode, also higher order modes are visible in transmission. In particular the TEM00 corresponds to the higher peak, the one with an amplitude of ~ 1.7 V. The peak with an amplitude of ~ 0.25 V is the LG10 mode and it represents a mismatch of the beam in the cavity; the smaller peaks are the HG10 and HG01 modes and they corresponds to an incorrect alignment of the beam with respect to the cavity axis.

Furthermore, by zooming on one specific resonance peak, it was possible to notice that the signal was actually very noisy; indeed, the peaks were not characterized by the typical Lorentzian shape but they where instead very deformed, as visible in Figure 4.13.
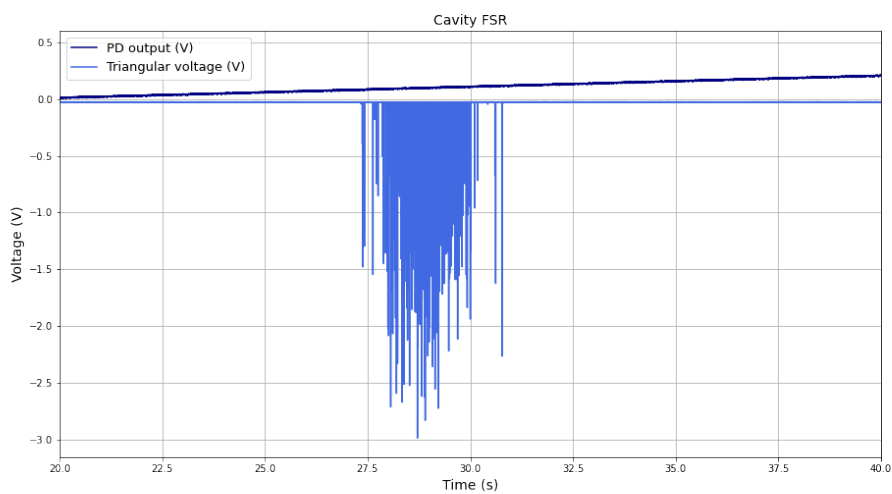

Figure 4.13: Plot of one of the TEM00 peaks transmitted by the cavity.

After some analysis on the cavity stability it was possible to attribute the cause of this noise to the relative motion of one mirror with respect to the other. For this reason the cavity structure has been changed a couple of times. The first revision of the design consisted in the reduction of the cavity length from 16 cm to 12 cm. In this way the pillars supporting the mirrors could be fixed together using two steel lateral plates in order to diminish their relative motion. This new design is visible in Figure 4.14. In this case the waist of the cavity's supported beam had to be equal to $w_0 = 269\,\mu m$. Using this arrangement it was noticed that the signal obtained scanning the cavity with the temperature control was still noisy.
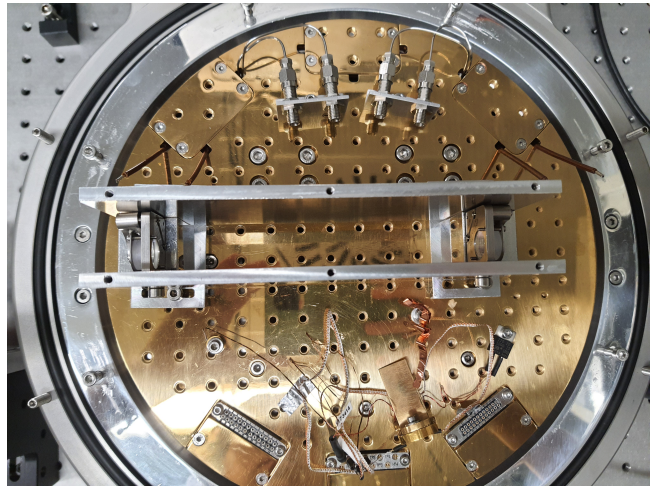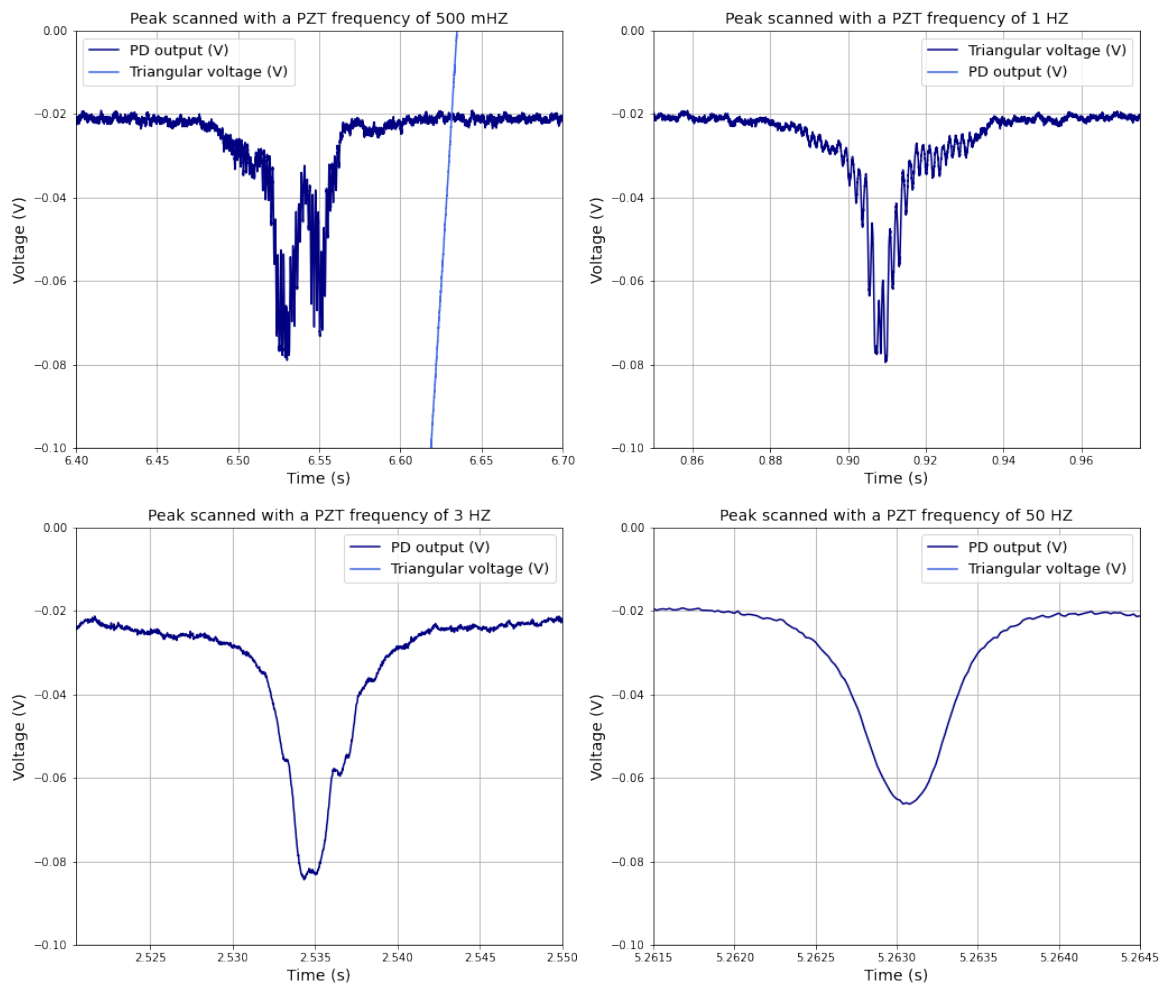

Figure 4.14: Picture of the second cavity.

Figure 4.15: Plot of one of the TEM00 peaks transmitted by the cavity when scanning the cavity at different frequencies.

However, the transmitted signal obtained by performing the cavity scan with the piezo actuator was disturbed only when the piezo scanning frequency was low, but it improved progressively when the scanning frequency was increased. This can be seen in the plots in Figure 4.15, where the scanning frequencies are 500 mHz, 1 Hz, 3 Hzand 50 Hz.

As the the fact of fixing the mirrors to each other has proven to be an effective solution, the stability of the cavity has been further improved by switching to an actual monolithic cavity (see Figure 4.16). This final cavity still has the length of 10.6 cm and the mirrors, instead to be screwed on two independent pillars, are mounted on the same robust base. This base is basically a rectangle block of aluminum with the threaded holes to fix in a rigid way the mirrors, the piezo actuator and the membrane.
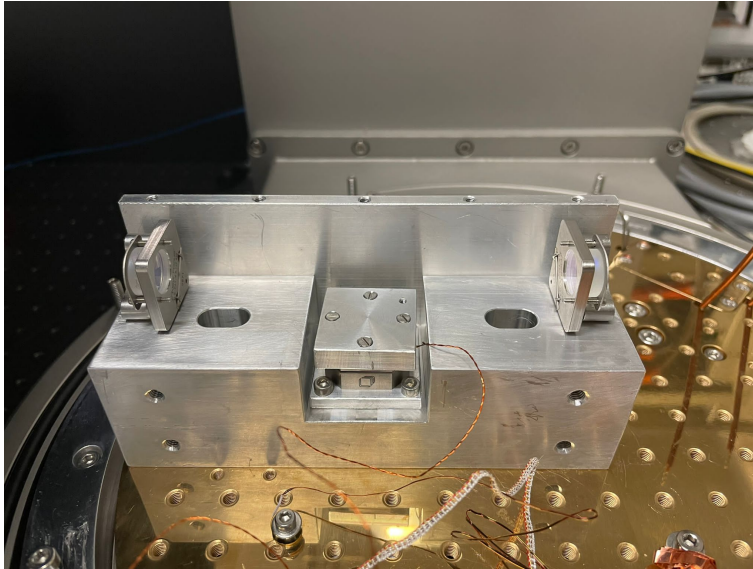

Figure 4.16: Picture of the final design: the monolithic cavity.
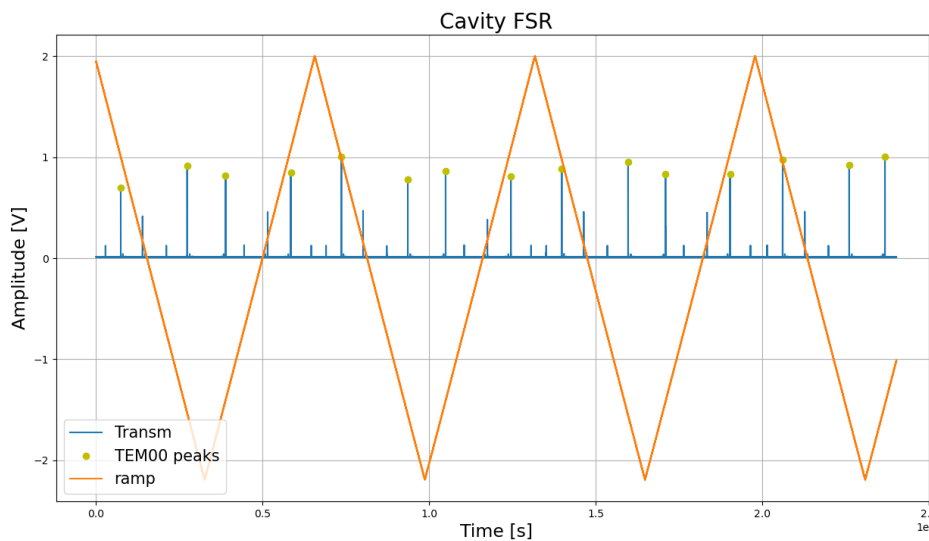

Figure 4.17: Signal transmitted by the monolithic cavity when acting on the temperature control.

The signal used to study the free spectral range of this cavity, obtained acting on the temperature

control of the laser, is plotted in Figure 4.17. The signal has been processed and only the TEM00 peaks are selected; calculating the distance between the TEM00 peaks corresponding to the same ramp it is possible to obtain the free spectral range. The expected value is $FSR = 1.41$ GHz, and the experimental value obtained is $FSR = 1.42 \pm 0.03$ GHz.

To correctly analyze the width of the TEM00 peak, the cavity has been scanned acting on the piezo actuator with a triangular signal with a frequency of 8 Hz. The transmitted signal is visible in Figure 4.18.
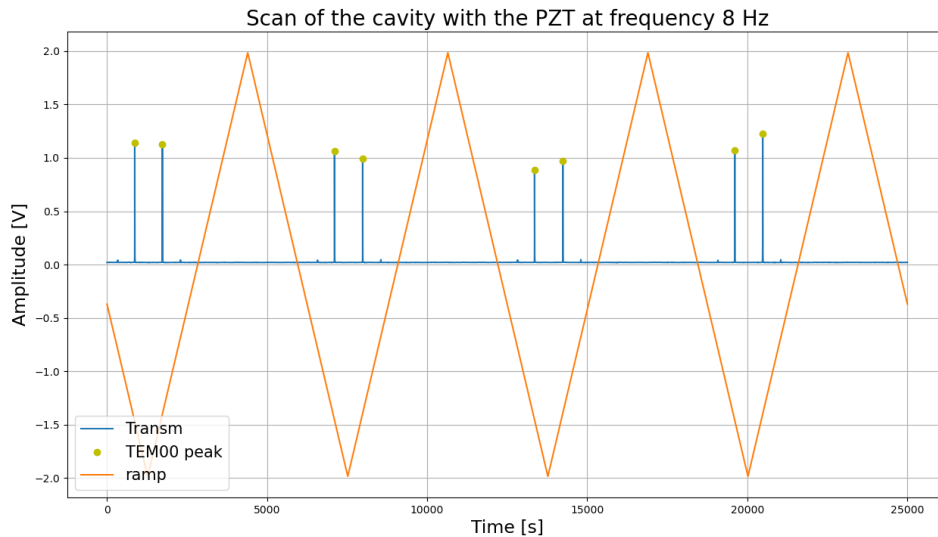

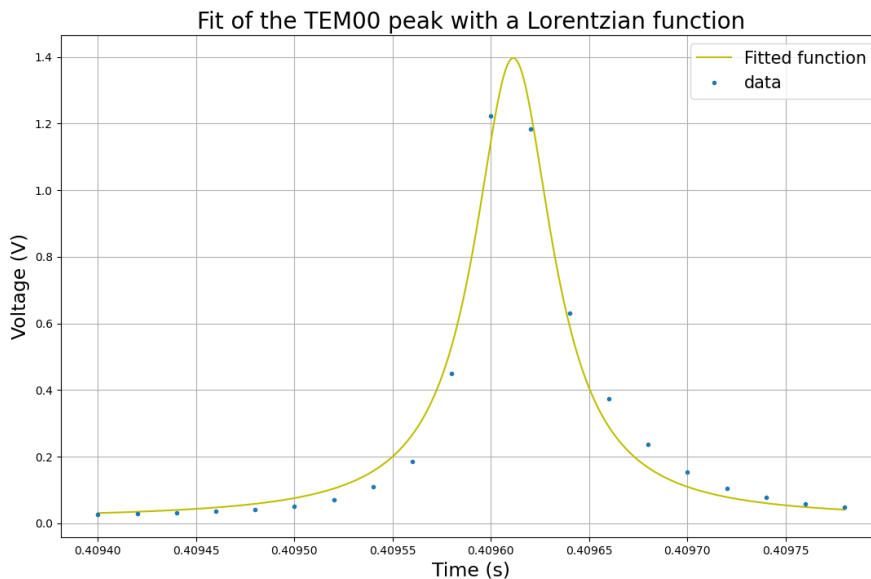Figure 4.18: Signal transmitted by the monolithic cavity when acting on the piezo actuator.

Figure 4.19: The plot shows the fit of one of the TEM00 peaks performed with a Lorentzian function.

Also in this case the data have been processed in order to identify the TEM00 peaks, fit them

with a Lorentzian function and obtain their full width at half maximum. One of the fitted peaks is shown in Figure 4.19 as an example.

The full width at half maximum results to be $\delta\nu = 0.060 \pm 0.008$ MHz.

The value of the finesse obtained experimentally is therefore $\mathcal{F} = 23621 \pm 3183$, while the value of the theoretical finesse is $\mathcal{F}_{th} = 15706$.

This inconsistency between the two finesse values could be do to the fact that the transmitted peaks have not exactly the shape of a Lorentzian curve, but instead one of their sides has a more exponential shape. This could be due to the frequency scan performed by the piezo actuator, that causes a deformation of the peak shape [19]. This results in a smaller width and therefore in a higher finesse value. Nevertheless, The finesse value obtained experimentally is in good agreement with the finesse value measured during an other experiment where a different optical cavity had been built using the same mirrors.

Chapter 5

Optical losses measurement

5.1 Membrane positioning and alignment

As already explained in subsection 3.3.2, a system of two coupled cavities is created when the membrane is placed in the middle of the Fabry-Perot. As explained above the correct alignment of the laser with the optical axis of the cavity is mandatory to match the resonance of the TEM00 mode inside the resonator. When the membrane is placed within the resonator it has to be properly aligned as it is crucial to have the membrane perpendicular to the beam propagation direction inside the cavity. Indeed, only in this way the losses due to scattering are minimized and the actual absorption coefficient of the membrane can be measured.
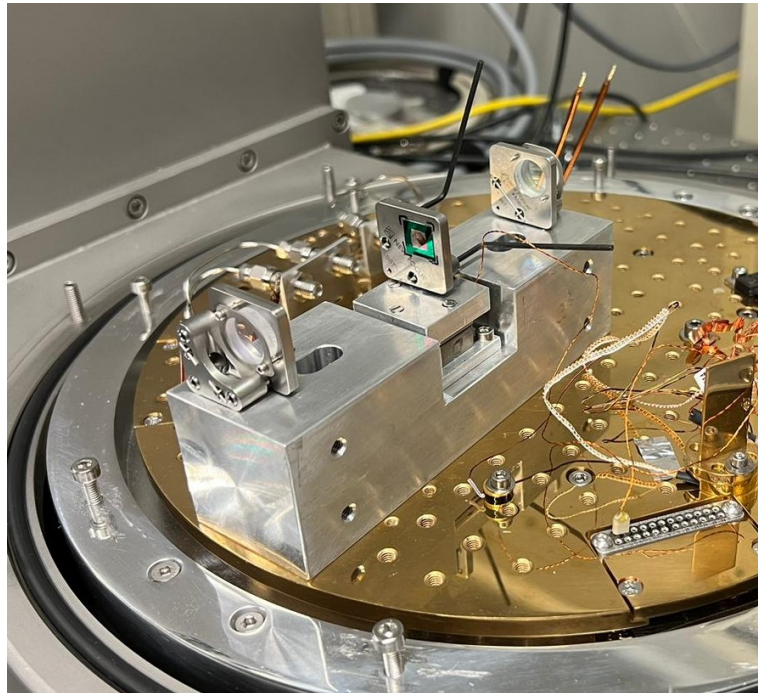

Figure 5.1: Membrane alignment inside the cavity

A red laser can be used as a tracer to roughly set the correct alignment of the membrane in the cavity.
The most appropriate way to use the red laser would imply to inject it in the optical fiber alongside the infrared laser: in this way the two beams would be already aligned at the fiber output and the red laser would follow exactly the path of the infrared one. Unfortunately, the available space on

the optical bench that host the fiber injection port was not sufficient to install the necessary lenses and mirrors to couple the red laser to the fiber. For this reason, during the alignment process, the red laser has been placed at the cavity output, in place of the CCD. In this way the red beam enters the cavity from the back mirror and it follows the same optical path of the infrared beam but in the opposite direction.

The membrane angle with the cavity axis can be adjusted using the three screws on its mount and it can be considered correctly aligned when the red beam exiting from the cavity goes through all the elements of the optical line and overlaps with the infrared laser at the optical fiber output. At this point the transmitted signal from the cavity can be employed to adjust even more precisely the membrane angle: when the resonance peak amplitude is maximized, the membrane alignment is optimized.

This operation is not straightforward because the screws that tilt the membrane are not very precise and easy to regulate by hand; the process will be way more accurate when the membrane will be fixed on the motorized tip-tilt.

Regarding instead the movement of the membrane along the optical axis of the cavity, it is realized with the Attocube piezo actuator which at a temperature of 300 K covers a range of $80\,\mu m$ when a voltage of 60 V is supplied.

The quadrant photodiode PDQ30C has been used to verify the correct functioning of the piezo actuator. The PDQ30C is an Indium-Gallium-Arsenide (InGaAs) photodiode and it can be used for precise path alignment of light in the 1000 to 1700 nm range. The sensor is segmented into four separate active areas that outputs three analog voltages. The X-axis and Y-axis signals are proportional to the power difference sensed by the left-minus-right and top-minus-bottom pairs of photodiode elements in the detector array; the SUM signal is proportional to the total amount of light falling on the sensor. A clarifying image of the sensor is shown in Figure 5.2 while the corresponding equations are the following:

Figure 5.2: Scheme of the QPD sensor

$$x_{axis} = (Q2 + Q3) - (Q1 + Q4)$$
$$y_{axis} = (Q1 + Q2) - (Q3 + Q4)$$
$$SUM = (Q1 + Q2 + Q3 + Q4)$$

The red laser has been used again for this operation. In particular the red laser has been placed outside the cryostat (as shown in the scheme in Figure 5.3) in such a way to have the beam impinging on the membrane at a 45° angle. In the same way, the quadrant photodiode has been placed on the other side of the cryostat in the correct position to detect the beam reflected by the membrane at the angle of 45°. With this arrangement, when a certain voltage is supplied to the piezo actuator, the membrane is displaced along the axis of the cavity and the reflected red beam hit the quadrant photodiode sensor in a different position every time. The signal produced by the photodiode is studied using an oscilloscope.

A precise characterization of the piezo actuator has not been done yet. However,using this method, it has been seen that the effect of the piezo start to be significant when the supplied voltage is greater the $20V$, while for lower voltages the membrane motion is not detectable with the quadrant photodiode.
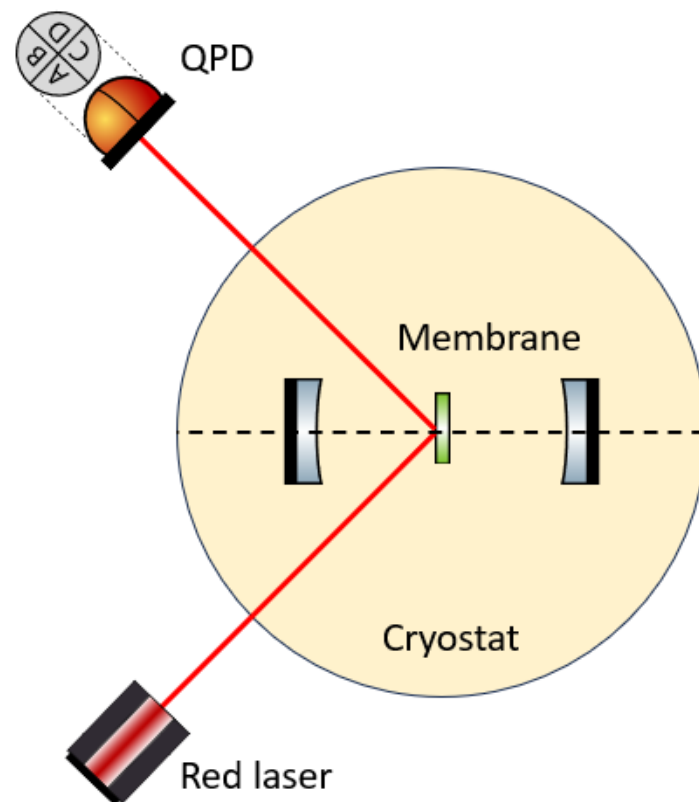
Figure 5.3: Scheme of the arrangement used to verify the proper functioning of the piezo actuator.

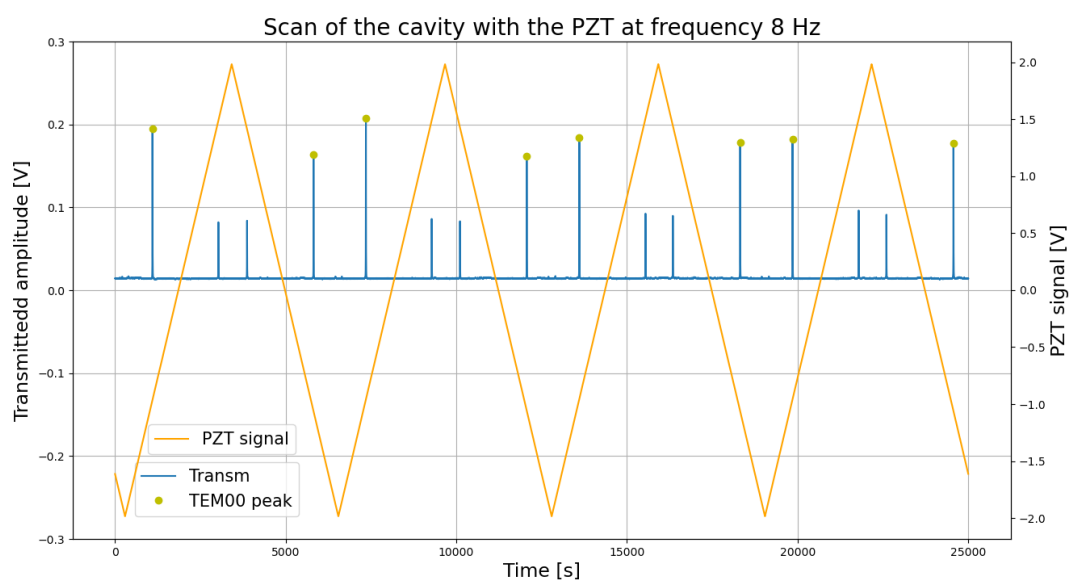## 5.2   Measurement of the finesse modulation

Figure 5.4: Signal transmitted by the cavity with the membrane in the middle.

The method used to measure the finesse of the cavity with the membrane in the middle is equal to the one used in for the empty cavity and already described in subsection 4.2.3. As the reflectivity of the membrane is very low ($r_m^2 \simeq 0.0003$) it is possible to assume that the free spectral range of the cavity does not change when the membrane is placed between the mirrors and, in the same way, it does not change when the membrane is displaced inside the cavity.

To evaluate how the finesse varies according to the membrane position, the width of the resonance peak is measured every time the membrane is shifted inside the cavity by means of the piezo actuator. As it was done previously, the width of the TEM00 peak is evaluated byfitting the transmitted signal from the cavity when it is scanned by the piezo acting on the laser crystal.

As it can be seen in Figure 5.4, the amplitude of the transmitted peaks is much lower when the membrane is present in the cavity. This is primarily an effect of the membrane absorption, but almost certainly also the losses due to scattering can be consistent if the membrane is not properly aligned.

In the Table 5.1 are outlined the values obtained for the TEM00 peak width, for the TEM00 peak amplitude and for the finesse when the position of the membrane is changed by varying of ~ 0.2 V the voltage sent to the piezo actuator of the membrane.

V_{PZT} (V)	FWHM (MHz)	σ_{FWHM} (MHz)	Ampl (V)	σ_{Ampl} (V)	Finesse	$\sigma_{Finesse}$
28.85	0.13	0.013	0.185	0.012	10850	1076
28.95	0.139	0.012	0.151	0.007	10197	916
29.05	0.17	0.04	0.106	0.009	8095	1918
29.15	0.2	0.03	0.072	0.003	6997	923
29.25	0.23	0.06	0.068	0.002	5947	1401
29.34	0.18	0.02	0.081	0.004	7773	997
29.58	0.21	0.05	0.082	0.005	6477	1501
29.77	0.2	0.05	0.08	0.004	7014	1779

Table 5.1: Values of the FWHM and amplitude of the TEM00 peak and of the cavity finesse measured for different positions of the membrane in the cavity.

To better understand the behaviour of the three tabled quantities, their variations are plotted in Figure 5.5, Figure 5.6 and Figure 5.7. From these plots it is evident that all the three studied quantities are characterized by a certain variation when the position of the membrane changes. Unfortunately the expected finesse behaviour predicted in subsection 3.3.2 is not visible yet and for this reason it has not been possible to estimate the absorption coefficient of the membrane. Anyway the value of the finesse is reduced to a value comparable to the one expected from the simulation presented in subsection 3.3.2.

Furthermore it is possible to confirm that the TEM00 peak transmitted from the cavity widens when the membrane is present in the cavity. It is also possible to notice that when the FWHM increases, and therefore the losses are higher, the amplitude of the peak diminishes as expected.

One of the reason for the defective outcome of the measurement could be attributed to the non-precise controlling of the piezo actuator. As it is well-known, piezo-actuators can display phenomena such as hysteresis and creep. Due to the fact that the procurement of such actuator suffered of considerable delays, it has not been possible to perform an extensive characterization of its working behavior, nor to implement more sophisticate control systems such as feedback loops etc. However, the preliminary characterization reported in figure 5.3 suggests that the actuator is not correctly positioning the membrane, altering the results of the experiment.

A second step that has to be done to fix the measurement is the improvement of the membrane alignment. Indeed, the membrane perpendicularity with respect to the beam propagation direction should be checked and adjusted every time it is displaced with the piezo. However, this has not

been done during this data taking because the motorized tip-til-mount was not available yet in the laboratory. This further correction could certainly reduce the scattering losses and therefore make the measurement more accurate.
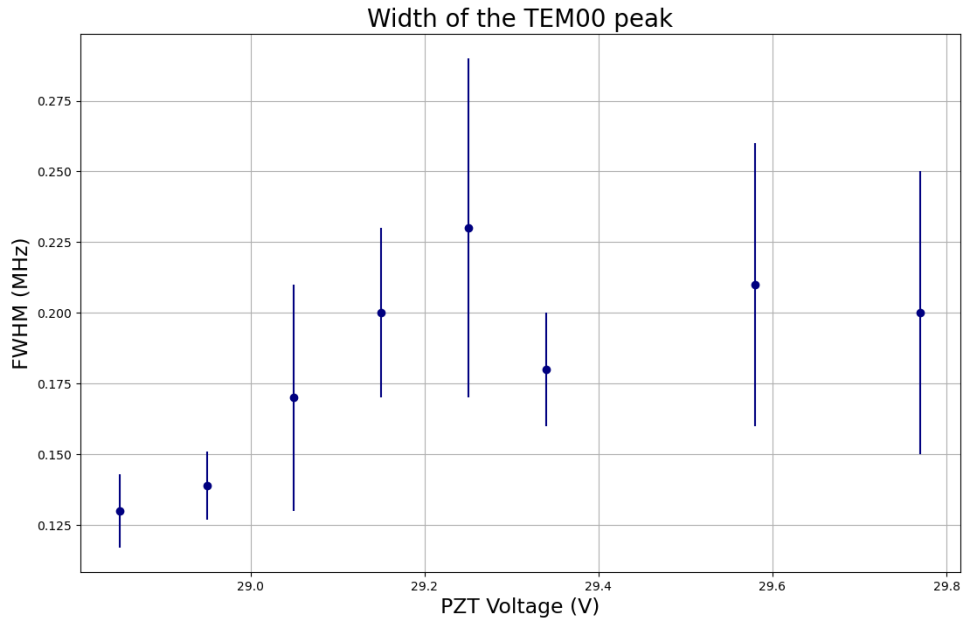

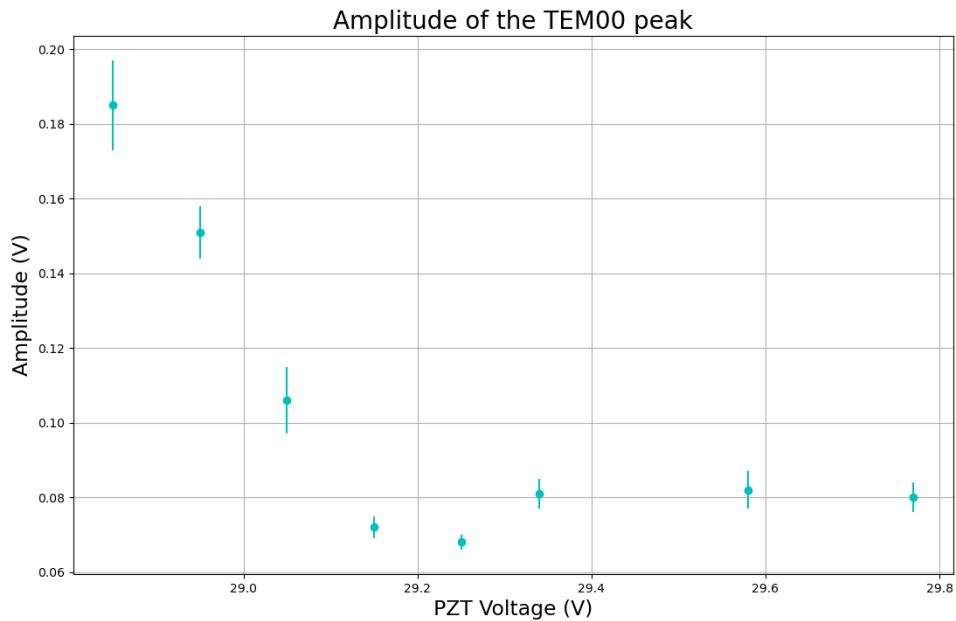Figure 5.5: Variation of the width of the TEM00 peak transmitted through the cavity.

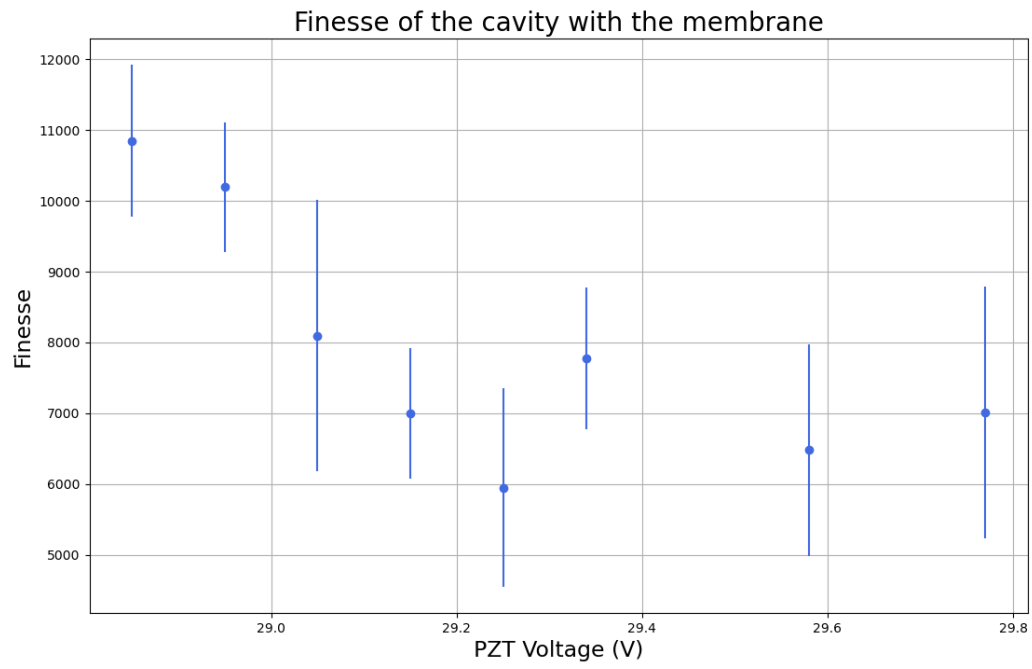Figure 5.6: Variation of the amplitude of the TEM00 peak transmitted through the cavity.

Figure 5.7: Variation of the cavity finesse.

Chapter 6

Conclusions

During this thesis, it has been developed an apparatus for the simultaneous and direct characterization of the mechanical dissipation and the optical losses of materials used as coatings for high precision opto-mechanical experiments.

On difference with other setups existing in the gravitational wave community, this approach is based on characterizing the coatings not as deposited on a substrate but in form of freestanding membranes. This new scheme will allow to perform our characterizations without being affected by the interaction between the coating and the substrate. The apparatus will allow to measure the above mentioned quantities both at room temperature and at cryogenic temperature, both at atmospheric pressure and in vacuum.

At this stage, the essential optical setup required to conduct the measurement has been successfully designed and built. In particular, the characterization of the optical cavity, performed through the measurement of its principal parameters (the free spectral range and the finesse), has been achieved. Although the effect of the membrane in the cavity is visible and measurable, there are certain components and parameters within the setup that are still in need of optimization. This is for example the case of the piezo actuators that allow to displace and align the membrane inside the optical cavity. Indeed, their characterization will for certain allow to obtain more consistent results and a more evident modulation of the finesse. Thanks to these improvements it will be possible to provide an estimate of the silicon nitride optical absorption.

In the near future, the plan consists in integrating the necessary instrumentation to the already existing apparatus, to enable it to measure also the mechanical dissipations of the free-standing membranes. Once the characterization of the commercial SiN membranes will be completed, the objective of this research will be to produce and analyse homemade membranes to test new and promising coating materials.

Bibliography

[1] S.Carrol, *Spacetime and Geometry: An Introduction to General Relativity*. Cambridge University Press, 2019.

[2] M. Maggiore, *Gravitational Waves. Vol. 1: Theory and Experiments*. Oxford University Press, 2007.

[3] https://www.virgo-gw.eu/it/science/detector/sensitivity/

[4] https://www.ligo.caltech.edu/page/ligo-technology

[5] Saulson P.R., *Thermal noise in mechanical experiments*. Phys.Rev.D, 42, 2437-2445 (1990)

[6] Y. Levin, *Internal thermal noise in the LIGO test masses : a direct approach*. Phys.Rev.D57:659-663, 1998

[7] M Granata et al, *Amorphous optical coatings of present gravitational-wave interferometers*. Phys.Rev.D57:659-663, 1998

[8] S. Reid, I. W. Martin, *Development of Mirror Coatings for Gravitational Wave Detectors*. Academic Editor: Desmond Gibson, 2016

[9] G.Vajente, L. Yang et al, *Reduced Room Temperature Thermal Noise in Titania-Doped Germania Coatings for Gravitational Wave Detectors*. August 2021Physical Review Letters 127(7)

[10] G. M. Harry et al, *Thermal noise in interferometric gravitational wave detectors due to dielectric optical coatings*. Class. Quantum Grav. 19 (2002) 897–917

[11] A. Siegman, *Lasers*. University Science Books, (1986)

[12] G. R. Fowles, *Introduction to modern optics*. Dover Publications, New York, 1989

[13] Landau, L.D. and Lifshitz, *Theory of Elasticity*. Pergamon Press, New York, NY, 75-97.

[14] A. W. Leissa, *Vibration of plates*, 2013

[15] M. Fletcher et al, *Effect of Stress and Temperature on the Optical Properties of Silicon Nitride Membranes at 1,550 nm*. Front. Mater., 31 January 2018, Sec. Optics and Photonics

[16] A. A. Darki, *Mechanical investigations of free-standing SiN membranes patterned with one-dimensional photonic crystal structures*, Journal of Applied Physics 131, 195101 (2022)

[17] J. Steinlechner et al., *Optical absorption of silicon nitride membranes at 1064 nm and at 1550 nm*, Phys. Rev. D 96, 022007, 2017

[18] J. Steinlechner et al., *Silicon-Based Optical Mirror Coatings for Ultrahigh Precision Metrology and Sensing*, Phys. Rev. Lett. 120, 263602, 2018

[19] M. J. Lawrence et al., *Dynamic response of a Fabry–Perot interferometer*, 1999 Optical Society of America